Acta Pharmaceutica Sinica B 2022;12(9):3618–3638

Chinese Pharmaceutical Association
Institute of Materia Medica, Chinese Academy of Medical Sciences

Acta Pharmaceutica Sinica B

www.elsevier.com/locate/apsb
www.sciencedirect.com

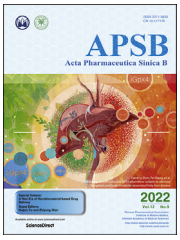

ORIGINAL ARTICLE

Inhibition of ASCT2 induces hepatic stellate cell senescence with modified proinflammatory secretome through an IL-1α/NF-κB feedback pathway to inhibit liver fibrosis

Feixia Wang[a], Zhanghao Li[a], Li Chen[a], Ting Yang[a], Baoyu Liang[a], Zili Zhang[a], Jiangjuan Shao[a], Xuefen Xu[a], Guoping Yin[c], Shijun Wang[d], Hai Ding[b], Feng Zhang[a,*], Shizhong Zheng[a,*]

[a]*Jiangsu Key Laboratory for Pharmacology and Safety Evaluation of Chinese Materia Medica, School of Pharmacy, Nanjing University of Chinese Medicine, Nanjing 210023, China*
[b]*Department of General Surgery, Nanjing Hospital Affiliated to Nanjing University of Chinese Medicine, Nanjing 210003, China*
[c]*Department of Anesthesiology, Nanjing Hospital Affiliated to Nanjing University of Chinese Medicine, Nanjing 210003, China*
[d]*College of Traditional Chinese Medicine, Shandong University of Traditional Chinese Medicine, Jinan 250035, China*

Received 31 December 2021; received in revised form 14 February 2022; accepted 25 February 2022

KEY WORDS

Hepatic stellate cells;
Senescence;
SASP;
ASCT2;
Precursor IL-1α;
NF-κB;
Atractylenolide III;
Liver fibrosis

Abstract Senescence of activated hepatic stellate cells (aHSCs) is a stable growth arrest that is implicated in liver fibrosis regression. Senescent cells often accompanied by a multi-faceted senescence-associated secretory phenotype (SASP). But little is known about how alanine-serine-cysteine transporter type-2 (ASCT2), a high affinity glutamine transporter, affects HSC senescence and SASP during liver fibrosis. Here, we identified ASCT2 is mainly elevated in aHSCs and positively correlated with liver fibrosis in human and mouse fibrotic livers. We first discovered ASCT2 inhibition induced HSCs to senescence *in vitro* and *in vivo*. The proinflammatory SASP were restricted by ASCT2 inhibition at senescence initiation to prevent paracrine migration. Mechanically, ASCT2 was a direct target of glutaminolysis-dependent proinflammatory SASP, interfering IL-1α/NF-κB feedback loop *via* interacting with precursor IL-1α at Lys82. From a translational perspective, atractylenolide III is identified as ASCT2 inhibitor through directly bound to Asn230 of ASCT2. The presence of −OH group in atractylenolide III is suggested to be favorable for the inhibition of ASCT2. Importantly, atractylenolide III could be utilized to

*Corresponding authors.
E-mail addresses: 300631@njucm.edu.cn (Feng Zhang), nytws@njucm.edu.cn (Shizhong Zheng).

https://doi.org/10.1016/j.apsb.2022.03.014
2211-3835 © 2022 Chinese Pharmaceutical Association and Institute of Materia Medica, Chinese Academy of Medical Sciences. Production and hosting by Elsevier B.V. This is an open access article under the CC BY-NC-ND license (http://creativecommons.org/licenses/by-nc-nd/4.0/).

treat liver fibrosis mice. Taken together, ASCT2 controlled HSC senescence while modifying the proinflammatory SASP. Targeting ASCT2 by atractylenolide III could be a therapeutic candidate for liver fibrosis.

© 2022 Chinese Pharmaceutical Association and Institute of Materia Medica, Chinese Academy of Medical Sciences. Production and hosting by Elsevier B.V. This is an open access article under the CC BY-NC-ND license (http://creativecommons.org/licenses/by-nc-nd/4.0/).

1. Introduction

Liver fibrosis, which is characterized by excess extracellular matrix (ECM) deposition, progressively constrains normal liver regeneration, increases the risk of liver failure, and generates a sustained microenvironment for the development of liver cancer[1]. In liver injury, retinoid droplet-storing quiescent hepatic stellate cells (qHSCs) transdifferentiate into myofibroblast (MF)-like, activated HSCs (aHSCs)[2]. HSCs-derived MFs are the main cell type that produces ECM, and are considered the central driver of liver fibrosis[3]. Recent reports have demonstrated that activated HSCs are removed from the liver by undergoing either apoptosis or deactivation contributing to fibrosis resolution[4]. We previously reported that inhibition of activated HSCs is a regulated process, involving inhibition of pericyte[5], proinflammatory[6], glycolytic and contractile functions[7,8], and induction of apoptosis[9], lipogenic phenotype[10], and ferroptosis[11], which contributed to liver homeostasis and liver fibrosis resolution. However, much less is known about what regulates the deactivation of HSCs in the context of senescence, which is an important priority for our current studies.

Cellular senescence refers to a state of stable cell cycle arrest in which proliferating cells become resistant to growth-promoting stimuli[12]. Activated HSCs can switch from proliferating, ECM-producing profibrotic cells to growth-arrested, and ECM-degrading antifibrotic cells by undergoing senescence that limits liver fibrosis[13,14]. Our previous studies supported induction of HSCs senescence was a novel therapeutic strategy for improving liver fibrosis[15,16]. In addition to growth arrest, a noteworthy feature of senescent cells is the ability to secrete molecules, including proinflammatory cytokines, proteases, growth factors, or angiogenesis factors, termed as the senescence-associated secretory phenotype (SASP)[17]. SASP gene transcription is temporally regulated[18,19], where the first wave of SASP factors such as TGFβ1 and TGFβ3 are typically immunosuppressive. In contrast, the second wave of the SASP often consists proinflammatory factors such as IL1β, IL-6, and IL-8[18,19]. SASP harbors the potential for multiple beneficial and detrimental paracrine effects on tissue homeostasis and biological processes[20,21]. Thus, it remains to be seen how deciphering the signaling pathways in regulating the SASP and revealing manipulated targets to harness senescence-associated effects as beneficial therapies for liver fibrosis.

Alanine-serine-cysteine transporter type-2 (ASCT2, encoded by SLC1A5), participates in glutaminolysis[22]. Glutaminolysis is the conversion of the amino acid glutamine into α-ketoglutarate, a TCA cycle intermediate, which is typically observed in cancer cells[23]. HSCs activate, or transdifferentiate to MFs demands rapid adaptation to meet a heightened energy need similar to cancer cells[24]. A comparison of the differentially expressed metabolic genes between qHSCs and aHSCs signified a shift toward glutaminolysis, and inhibition of glutaminolysis blocked accumulation of MFs and liver fibrogenesis in mice[25]. Emerging evidence implies that the impaired metabolic pathway, which leads to the imbalance of mitochondrial metabolites, could trigger cellular senescence[26]. There is a putative idea to classify ASCT2 as potential therapeutic target to HSC senescence phenotypes regulation, and to underlie their functions in health and disease. To do this, we used various pharmacological, molecular, genetic and computational approaches to reveal the issue *in vitro* and *in vivo*.

2. Materials and methods

2.1. Patient specimens

Human liver tissues progressed to hepatocellular carcinoma (HCC, $n = 12$) and adjacent non-tumorous tissues ($n = 3$) were harvested from February 2013 and June 2017 in Nanjing Hospital Affiliated to Nanjing University of Chinese Medicine (Nanjing, China). Paraffin liver sections were used for histology examination, α-SMA staining and ASCT2 staining. Histologically staged fibrosis [no fibrosis (F0/1), $n = 3$], mild fibrosis (F2, $n = 3$), severe fibrosis (F3−4, $n = 9$) were defined based on Scheuer criteria[27]. The study protocol was approved by the Medical Ethical Committee of Nanjing Hospital Affiliated to Nanjing University of Chinese Medicine. Informed consent in writing was obtained from patients. The specific characteristics of patients were described in our previous study[28]

2.2. Animal studies

Male ICR mice (18−20 g) were housed in an air-conditioned room at 25 °C with 12-h dark/light cycles. Mice received humane care with unlimited access to a chow diet and water during the whole study. Animal studies were approved by the Institutional and Local Committee on the Care and Use of Animals of Nanjing University of Chinese Medicine (approval number: 202009A043, Nanjing, China). All animals received humane care according to the National Institutes of Health (USA) guidelines. We complied with the principles of the 3Rs and respected the highest ethical and animal welfare standards in carrying out the animal experiments.

Liver fibrosis was induced by ligation of the common bile duct (BDL) or by intraperitoneal (i.p.) injections of carbon tetrachloride (CCl_4, Sigma, St. Louis, MO, USA)[29]. Briefly, for BDL, the mice were anesthetized by intraperitoneal injection of sodium pentobarbital (3%) 40 mg/kg, fixed in supine position on the operating table, and the surgical field was sterilized as debrided: The abdominal cavity was opened along the midline of the abdomen layer by layer, the common bile duct was found at the beginning of the duodenum and separated, and two 7-0 sutures were threaded below the common bile duct and ligated separately, and the bile duct was cut in the middle of the ligature, then the inner layer was sutured with 7−0 sutures and the outer layer was

sutured with 5−0 sutures, and the mice were placed on a heating pad to maintain the anal temperature at 37 ± 0.5 °C. The control group was not treated with ligation, and other operations were the same. Liver fibrosis was induced 14 days after surgery. For CCl_4, 10% CCl_4 with olive oil (CCl_4:olive oil = 1:9, *v*/*v*) were injected intraperitoneally three times a week at 0.5 μL/g mouse body weight for 8 weeks to induce mice liver fibrosis.

AAV8-ASCT2 shRNA and AAV8-scrambled shRNA (10^{11} pfu/mL) were synthesized by OBiO Technology (Shanghai, China) and was performed to CCl_4-challenged mice *via* tail vein. HSC-specified VA-Lip-ASCT2 shRNA and HSC-specified VA-Lip-ASCT2 plasmid were prepared according to a reported method and was performed to CCl_4-challenged mice *via* tail vein[30]. The used primer sequences are shown in Supporting Information Table S1. CCl_4-challenged mice (n = 66) were randomly divided into CCl_4, CCl_4+AAV8-scrambled shRNA, CCl_4+AAV8-ASCT2 shRNA, CCl_4+VA-Lip-ASCT2 shRNA, CCl_4+VA-Lip-ASCT2 plasmid, CCl_4+20 mg/kg atractylenolide III, CCl_4+30 mg/kg atractylenolide III, CCl_4+40 mg/kg atractylenolide III, CCl_4+0.25 mg/kg colchicine, CCl_4+40 mg/kg atractylenolide III + VA-Lip ASCT2 shRNA, CCl_4+40 mg/kg atractylenolide III + VA-Lip-ASCT2-plasmid. At the end of the Week 8, all animals were sacrificed, and the tissue and blood samples were harvested.

2.3. Cell culture studies

Human HSC cell line LX-2 (Cat. CL-0560) was purchased from Procell Life Science & Technology, rat HSC cell line T6 (Cat. GF010) was purchased from Shanghai GEFAN Biotechnology, human normal hepatocytes cell line LO2 (CL-0111) was purchased from Procell Life Science & Technology, and cells were cultured in Dulbecco's modified Eagle's medium (DMEM), supplemented with 10% foetal bovine serum (FBS) and 1% penicillin−streptomycin antibiotics.

Isolation of primary mouse HSCs, hepatocytes, and Kupffer cells was conducted as described previously[31]. Briefly, livers were digested with retrograde stepwise perfusion with solutions containing pronase (Sigma−Aldrich, 11459643001) and collagenase (Sigma−Aldrich, 11213865001). The obtained cells were centrifuged and washed with Gey's balanced salt solution B (GBSS/B) buffer and centrifuged at 50 × *g* for 10 min, to eliminate the majority of hepatocytes. After hepatocytes were pelleted, the non-parenchymal cells (NPC)-enriched precipitates were further centrifuged at 1500 × *g* for 15 min. GBSS/B solution containing 10% Nycodenz were added to the non-parenchymal cells and centrifuged at 1500 × *g* for 15 min to separate primary HSCs. The above Nycodenz layer was aspirated, 50% Percoll was added and centrifuged at 1500 × *g* for 15 min to obtain primary Kupffer cells. Cells were cultured in DMEM containing 10% FBS.

2.4. Reagents and chemicals

Etoposide (S122508, chemotherapeutics agent) was obtained from Selleck (Shanghai, China), the concentration used is 5 mmol/L *in vitro*. Benser (13910, an inhibitor of ASCT2) was obtained from Sigma−Aidrich (Merck, USA), the concentration used is 10 μmol/L *in vitro*. DM-α-KG (349631, agent for α-KG supplement) was obtained from Sigma−Aldrich (Merck, USA), the concentration used is 50 μmol/L or 100 μmol/L *in vitro*. L-Glutamine (HY-N0390, agent for glutamine supplement), L-serine (HY-N0650, agent for serine supplement), L-asparagine (HY-N0667, agent for asparagine supplement), L-threonine (HY-N0658, agent for threonine supplement) were obtained from MedChemExpress (Shanghai, China), the concentration used is 100 μmol/L *in vitro*. 4-OHT (HY-16950, agent to induce SASP production) was purchased from MedChemExpress (Shanghai, China), the concentration used is 100 μmol/L *in vitro*. PDTC (HY-18738, an inhibitor of NF-κB), the concentration used is 100 μmol/L *in vitro*. Atractylenolide III (HY-N0203, Drug) was purchased from MedChemExpress (Shanghai, China), the concentration used is 20, 30 or 40 μmol/L *in vitro*, the concentration used is 20, 30 or 40 mg/kg *in vivo*. Atractylenolide I (T5S0167, Drug), atractylenolide II (T5S0168, Drug) were purchased from Topscience (Shanghai, China), the concentration used is 20, 30 or 40 μmol/L *in vitro*. Colchicine (HY-16569, agent for positive control) was purchased from MedChemExpress (Shanghai, China), the concentration used is 0.25 mg/kg *in vivo*. Recombinant human IL-1α protein (200-LA, protein for addition of IL-1α) was purchased from Bio-Techne (R&D Systems, Shanghai, China), the concentration used is 20 ng/mL *in vitro*.

2.5. Cell transfection

ASCT2 siRNA (Cat. sc-60210) or ASCT2 shRNA (Cat. sc-60210-SH) were from Santa Cruz Biotechnology Inc. (USA). ASCT2 overexpressing plasmid was synthesized by OBiO Technology (Shanghai, China). ASCT2-WT plasmid and ASCT2-N230G mutation plasmid were synthesized by KeyGEN Technology (Nanjing, China). IL-1A siRNA was synthesized by Tsingke Biotechnology (Beijing, China). Luciferase reporter plasmid containing four NF-κB-binding sites (#111216) was purchased from Addgene Plasmid. The used primers sequences were shown in Table S1. Transfections were performed with Lipofectamine RNAiMAX Transfection Reagent (13778150, Invitrogen, Carlsbad, CA, USA) according to the manufacturer's recommendations.

2.6. Senescence associated SA-β-Gal activity

SA-β-Gal staining was performed at pH 5.5 for mouse tissues and pH 6.0 for HSCs as previously described[32]. Briefly, frozen liver sections or adherent cells were fixed with 0.5% glutaraldehyde in PBS for 15 min, washed with 1 × PBS supplemented with 1 mmol/L $MgCl_2$ and stained for 5−8 h in 1 × PBS containing 1 mmol/L $MgCl_2$, 1 mg/mL X-Gal and 5 mmol/L potassium ferricyanide and potassium ferrocyanide. The slides were subsequently rinsed in 1 × PBS and mounted for determination. For quantification, 3−5 representative images of each sample were quantified using Image J.

2.7. Analysis of cell-cycle disruptions

Adherent cell samples were trypsinized and washed with PBS. The cell cycle was then detected using the Cell Cycle Detection Kit (KGA512) according to the protocol. Briefly, adherent cells were washed with 1 × PBS, and digested with EDTA-free trypsin and collected, centrifuged at 2000 rpm for 5 min using Eppendorf centrifuge (Germany), then fixed with 70% ice ethanol at 4 °C for 2 h, washed with 1 × PBS and stained with propidium iodide (PI) to assess DNA content, and the cells were measured on a FACS LSR II system (BD BioSciences, USA) at 488 nm wavelength. The cell cycle distribution analysis was performed using FlowJo software (v. 10.3).

2.8. Click-TM EdU incorporation assay

For the EdU assay, 10 μmol/L 5-ethynyl-2′-deoxyuridine (EdU) was incorporated into cells for 4 h. Harvested cells were submitted to the Click-TM EdU reaction according to the manufacturer's protocols (Beyotime biotechnology, C0085L). The absorbance was recorded in 450 nm for quantification.

2.9. RNA sequencing

Total RNA was extracted using TRIzol reagent (Invitrogen, Thermo Fisher, USA) from the senescent LX2 cells treated with shRNA targeting ASCT2 (shASCT2) or etoposide or the proliferating LX2 cells treated with scrambled control using. RNA samples were assessed for quantity and quality using a NanoDrop UV spectrophotometer (Thermo Fisher, USA) and a Bioanalyser (Agilent, USA). The library construction and sequencing were performed by sequences obtained from Shanghai Personal Biotechnology Co., Ltd. The data were obtained for three biological replicates per group, and aligned to the reference human genome version GRCh38.p10. The raw counts were accessed from the resulting bam files using the feature counts. RSEM software was used to estimate gene levels, read counts and FPKM values. DESeq2 was used to assess the significance of expression differences between the two experimental groups.

2.10. GSEA assay

Gene set enrichment assay (http://software.broadinstitute.org/gsea/index.jsp) was used for the contrast in pre-ranked mode utilizing the DESeq2 statistic as the ranking metric. This is a computational method for determining whether the defined genes show statistical significance and concordant differences between two biological states. *P* values were calculated using a bootstrap distribution created by resampling gene sets of the same cardinality.

2.11. Metabolite determination

Whole cell lysates of HSCs were prepared for measurements of glutamine, α-ketoglutarate (α-KG), citrate, malate, fumarate and succinate levels using the following ELISA kits: Human Glutamine ELISA Kit (JL19428), Human α-KG ELISA Kit (JL48612), Human Citrate ELISA Kit (JL48732), Human Malate ELISA Kit (JL45065), Human Fumarate ELISA Kit (JL47459), and Human Succinate ELISA Kit (JL48389). The absorbance at 450 nm was measured using a microplate reader (Bio-Rad, Hercules, CA, USA) and the concentrations of indicators were calculated from the respective standard curves. Cellular glutamate and GSH were detected in lysates by using Glutamate Assay Kit (BB-47344-1) and GSH Assay Kit (BB-4711-1) from BestBio (Shanghai, China) according to the manufacturer's protocols. Levels of glutamate and GSH were normalized to cellular protein amount.

2.12. Extracellular flux analyses (seahorse)

Experiments were carried out on Seahorse XF24 bioanalyzer (Agilent, USA). The oxygen consumption rate (OCR) was measured as described following the Mito Stress Assay Kit (Cat. 103674-100). Briefly, a total of 5×10^4 cells were seeded per well onto XF24 Cell-Tak (BD Bioscience, Cat. 354240), and cultured in growth medium for 12 h. And measurement was collected following incubation with Seahorse XF DMEM media supplemented with glutamine, sodium pyruvate, and glucose. And the 1.5 μmol/L ATP synthase inhibitor of complex V (oligomycin), 1.0 μmol/L mitochondrial uncoupler (FCCP) and 0.5 μmol/L ETC inhibitors of complexes I and III (rotenone with antimycin A) were injected from the XF24 ports as indicated to examine the basal respiration rate and maximum respiration rate. The analysis was performed using Seahorse Wave software (v. 2.6.3).

2.13. Co-immunoprecipitation (Co-IP)

For Co-IP analysis of ASCT2 and IL-1α interaction, we followed the protocol as our described previously[33]. rProtein A/G Plus MagPoly Beads (RM09008, ABclonal) were used in this assay. Briefly, cells were lysed with 1 mL lysis buffer containing protease inhibitors for 10 min at 4 °C, and centerfield at 12,000 rpm for 15 min using Eppendorf centrifuge (Germany). Then the protein concentrations were measured in Nano Drop, and equal amounts of cells lysate were used for Co-IP. Firstly, cell lysate was incubated with ASCT2 or IL-1α antibody at 4 °C for 2 h. Then the complex was incubated with pre-treated rProtein A/G Plus MagPoly Beads at 4 °C for 24 h. Finally, the precipitants were washed three times, and the immune complexes were eluted with sample buffer for 15 min at 95 °C. The immunoprecipitated proteins were subsequently separated by SDS-PAGE, followed by Western blot assay.

2.14. In vitro GST-pull down assay

For determining the ASCT2 and IL-1α interaction *in vitro*, GST-tagged IL-1α was expressed in 293 T cells. All sequences of oligonucleotides for preparation of various short RNA probes for mapping the IL-1α were as follows: FL, full length 1−271; F1, domain 1−112; F2, domain 112−271; F3, NLS domain (80−88) deletion; F4, K82N mutation. Approximately 8×10^6 cells were washed twice with PBS, harvested and lysed in cell lysis buffer plus complete protease inhibitor cocktail. The cellular supernatants were pre-cleared with glutathione-Sepharose 4B beads (GE Healthcare), and incubated with beads containing GST fusion proteins. The pull-down complex was boiled in SDS-PAGE loading buffer and analyzed by Western blot.

2.15. NF-κB reporter assays

NF-κB activity was determined using the NF-κB reporter plasmid and normalized based upon transfection efficiency using pRL-Tk *Renilla* luciferase reporter vector. Plasmids were co-transfected using Lipofectamine RNAiMAX Transfection Reagent into HSC-LX2 cells. NF-κB activity was assayed for luminescence using Dual-Luciferase Reporter Assay Kit (Yeasen Biotechnology, Shanghai, China) according to the manufacturer's protocols. Luminescence was measured using a Glo-Max Multilabel Reader (PerkinElmer, USA).

2.16. Biochemical analyses

Measurement of serum aspartate aminotransferase (AST), alanine aminotransferase (ALT) and direct bilirubin (DBIL) concentrations were determined using AU480 (Beckman Coulter, USA) according to the manufacturer's instructions.

2.17. Liver hydroxyproline content assay

Hydroxyproline (Hyp) content in livers was determined according to the Hyp assay kit's instruction manual. Hyp kit (A030-2-1) was purchased from Jiangcheng (Nanjing, China). The data is expressed as Hyp (μg) per liver weight (g).

2.18. Enzyme-linked immunosorbent assays (ELISA)

ELISA kit for intracellular IL-1α secretion (ab178008) was bought from Abcam (Shanghai, China). ELISA kit for mouse laminin (LN) (ml002126), mouse procollagen III (PC-III) (ml038007), hyaluronic acid (HA) (ml037445) and type IV collagenase (IV-C) (ml038234) were bought from Shanghai Enzyme-linked Biotechnology Co., Ltd. (Shanghai, China). ELISA assays were established according to the protocols.

2.19. Histological hematoxylin-eosin (H&E), sirius red and masson staining

Liver specimens were pre-served in 4% paraformaldehyde and then dehydrated in a graded alcohol series. Then, the sections were embedded in paraffin blocks, cut into 5 μm-thick sections and placed on glass slides and were stained with hematoxylin−eosin (H&E), Sirius red, and Masson for histopathological study. H&E, Sirius red, and Masson images from 10 random fields of each section were taken and quantified with ImageJ software. The liver fibrosis stage was assessed by Ishak scale[34]. The percentage of the area of the section occupied by positive staining using Image J software.

2.20. Immunohistochemistry and quantification

Frozen liver sections were fixed in 4% paraformaldehyde (PFA) for 10 min and then washed 3 times with PBS. According to the above results, 3 sections were chosen from each group for immunohistochemistry analysis. Briefly, sections prepared on slides were first submitted to antigen retrieval by incubation in citrate buffer (pH 6.0) for 5 min at 108 °C and pretreated with 3% H_2O_2 in PBS for 15 min at room temperature followed by washing with PBS. Slides were subsequently incubated in 5% bovine serum albumin (BSA) blocking solution for 20 min. Next, the slides were treated with indicated primary antibody overnight at 4 °C. The slides were incubated with secondary antibody overnight at 4 °C. Subsequently, steps are 3,3′-diaminobenzidine (DAB) staining and 3 washes with PBST were performed, followed by incubation in permanent red working solution for 20 min. Finally, the images were monitored by microscope. All antibodies used are described in Supporting Information Table S2. The percentage of the area of the section occupied by positive staining using Image J software.

2.21. Immunohistofluorescence

For immunohistofluorescence, PFA-fixed cells or cryosections were permeabilized with 0.2% Triton X-100, and then incubated with a blocking buffer containing 3% BSA for 20 min. After that, the sections were incubated with the indicated primary antibodies overnight at 4 °C, and then a secondary antibody for 1 h at room temperature. The sections were then stained with 4′,6-diamidino-2-phenylindole (DAPI) (#KGA215, keyGEN) and examined with a confocal laser scanning microscope (Leica, Wetzlar, Germany). All antibodies used in IHF were shown in Table S2. The percentage of the positive staining cell of the section occupied by using Image J software.

2.22. Generation of conditioned media

To prepare conditioned media (CM), HSCs were cultured to reach 80% confluence in 10 cm dishes, and treated as indicated. Then the medium was replaced with fresh complete medium. Alternatively, cyclosporine A (10 μmol/L) was added to HSCs culture for 24 h before replacing the medium with fresh drug-free medium. Forty-eight hours later, the media were collected and filtered through 0.22 μm PES filter (Merck Millipore Ltd., USA) to remove cells and cellular debris. The media were used immediately or aliquoted and stored at −80 °C for later use for culture of HSCs.

2.23. Wound-healing and Transwell migration assays

For wound-healing migration assay, confluent monolayers of cells were wounded with a p20 pipette tip. The images were taken after PBS washes (time 0 h). The cells were cultured in serum-free medium. After two days, the images were taken again (time 48 h). Three separate fields were photographed for each plate. For Transwell migration assay, Transwell membrane (8 μm pore size, 6.5 mm diameter; Corning Costar) was used for assay. Briefly, 2.5×10^4 cells were plated in the top chambers. The top chambers were filled with serum-free medium and the bottom chambers were filled with migration-inducing medium (with 10% FBS). The filters were fixed with 4% paraformaldehyde after 24 h. The cells on the upper side of the membrane were scraped with a cotton swab and the cells on the bottom side of the membrane were stained with crystal violet. The membranes were washed with PBS and images were taken after drying out.

2.24. Cell viability assay

Cell viability was evaluated by MTT assay. Thiazolyl blue tetrazolium bromide (MTT) powder (M5655, Sigma−Aldrich) was used for determination. Briefly, HSCs were plated in a 96-well plate and exposed to indicate treatment. 20 μL 5 mg/mL MTT with 100 μL DMEM were added to each well and incubated at 37 °C in 5% CO_2 for 4 h. 150 μL DMSO was added to dissolve the blue crystals, then the plates were measured at 560 nm using the Multi-Detection Microplate Reader (Bio-Rad, Hercules, CA, USA).

2.25. LDH release assay

Lactate dehydrogenase (LDH) release assay kit (Beyotime, C0016) was used for cell cytotoxicity in treated HSCs. Absorption at 490 nm was detected for the quantification of lactate dehydrogenase activity by Microplate Reader (Bio-Rad, Hercules, CA, USA).

2.26. qPCR

Total RNA was extracted from cells using Trizol (Invitrogen, Thermo Fisher Scientific Inc., USA). cDNA was generated using Hifair II 1st Strand cDNA Synthesis Kit (Yeasen, Shanghai, China) according the manufacturer's instructions. qPCR was performed using SYBR Green PCR kit (Yeasen). Results were

normalized to mouse GAPDH or human GAPDH based on the threshold cycle (C_t) and relative fold change calculated by the $2^{-\Delta\Delta Ct}$ method. The sequences of primers for qPCR were listed in Supporting Information Table S3.

2.27. Subcellular fractionation

Nuclear/cytoplasmic fractionation was performed using Nuclear and Cytoplasmic Extraction Kit (Beyotime, P0027) according to the protocol. Briefly, adherent cells were washed with 1 × PBS, harvested and lysed in Cytoplasmic Protein Extraction A plus complete protease inhibitor at 4 °C for 15 min. Then added Cytoplasmic Protein Extraction A and mixed at 4 °C for 5 min. The cells lysis was centrifuged at 12,000 rpm (4 °C) for 10 min using Eppendorf centrifuge (Germany), and supernatants containing cytosolic proteins were collected. Pellets were resuspended in a nuclear extraction buffer containing protease inhibitor and then, incubated for 10 min at 4 °C in agitation and centrifuged for 10 min at 13,000 rpm (4 °C). Supernatants containing nuclear proteins were collected.

2.28. Western blot

Livers or cell lysates were prepared in RIPA buffer with proteinase inhibitors (Roche, Madison, WI, USA). Nuclear/cytoplasmic fractionation was prepared as above. After protein quantification using NanoDrop, the protein lysates were subjected to polyacrylamide gel electrophoresis and transferred onto PVDF transfer membranes, which were then blocked and exposed to the corresponding antibodies. The blots were visualized by enhanced chemiluminescence (GE Healthcare Life Sciences) and digital images and densitometry were performed using a Bio-Rad system. All antibodies are described in Table S2.

2.29. Molecular docking

The bind of atractylenolide III to ASCT2 (PDB: 6GCT) was modeled using GLIDE software (Schrödinger, LLC, New York, NY, USA). Prior to docking, the structure of ASCT2 was prepared with the built-in protein preparation wizard method. The atractylenolide III ligand was generated by ChemDraw and minimized by using MM2 force field. The ASCT2−atractylenolide III complex model was constructed using the standard precision mode method as described previously[5]. The top ten ranking conformations for atractylenolide III were chosen to calculate the binding free energy (ΔG) with Prime MM-GBSA mode. The highest scoring orientation was chosen for further analysis, and the results were visualized and rendered by PyMOL. Interaction patterns and their distribution probabilities for atractylenolide III binding to ASCT2 were conducted by the Desmond site. Mutation formats of ASCT2 were generated by modifying the corresponding sequences and homology modeling methods (Discovery Studio, v.16). To provide a stable conformation for the MD simulation and energy minimization of ASCT2-WT and ASCT2-N230G, proteins were conducted by the Gromacs (v. 2019.1) software with the GROMOS96 force field. The solvation system was equilibrated as follows: The Berendsen thermostat method and NPT ensemble equilibration phase were performed for 10 ns. After these equilibration procedures, RMSD simulations were performed for the two proteins for 50 ns, respectively. The results of the simulation were analyzed by calculating the root-mean-square deviation (RMSF) as described previously[34].

2.30. Cellular thermal shift assay (CETSA)

HSC-LX2 cells were incubated with or without atractylenolide III for 2 h, then the cells were collected and subjected to Cellular Thermal Shift Assay (CETSA) assay. Briefly, incubated cells were equally divided into 10 parts, each parts got heated for 3 min under different temperature (43, 46, 49, 52, 55, 58, 61, 64, 67, 70 °C), then the heated cells were put into −80 °C for 12 h, put into room temperature for 5 min, then repeated one more time. After that, cell lysates were extracted by centrifuged at 20,000 × g for 20 min. The level of ASCT2 was detected by Western blot.

2.31. Microscale thermophoresis analysis

His-tagged ASCT2-WT purified protein (100 nmol/L) or His-tagged ASCT2-N230G mutation purified protein (100 nmol/L) was mixed with 16 different concentrations of atractylenolide III (0.1526 μmol/L−5 mmol/L). In the dilution series, the highest concentration was chosen to be 1000-fold higher than that of the expected equilibrium dissociation constant (K_d). Briefly, purified ASCT2-WT protein or purified ASCT2-N230G mutation protein was labeled with RED dyes (MO-L018, NanoTemper Technologies). An aliquot (10 μL) of the serial concentration dilution of the non-labeled molecule (atractylenolide III) was mixed with 10 μL of the labeled ASCT2-WT protein or labeled ASCT2-N230G protein. Mixed samples were loaded into the capillaries, and microscale thermophoresis (MST) analysis was performed using Monolith NT.115 MST instruments (NanoTemper, Munich, Germany). Standard capillaries (Cat. K002, NanoTemper) were used in the experiments. The results were characterized and determined using MO. Affinity Analysis 3.

2.32. Statistical analysis

Data are expressed as mean ± standard error of mean (SEM). The significant difference of normally distributed data was determined by Student's t test (comparison between two groups) or one-way ANOVA with post hoc Tukey's test (comparison between multiple groups). For the non-normally distributed data, Mann−Whitney U test (comparison between two groups) or Kruskal−Wallis H test with *post hoc* Steel Dwass test (comparison between multiple groups) was used to determine the significant difference. Spearman analysis was used to determine the correlation. GraphPad Prism software version 7.0 (GraphPad Software, San Diego, CA, USA) was used. Statistical significance was considered where $P < 0.05$.

3. Results

3.1. Increased ASCT2 expression specifically in HSCs during liver fibrosis

We initially characterized the expression pattern of ASCT2 in human liver specimens with advanced liver fibrosis. H&E stains, Masson stains and α-SMA (the activated HSC marker) immunohistochemistry (IHC) showed the fibrotic progression (Fig. 1A). Notably, increased ASCT2 was demonstrated in the bridging fibrosis area in patients along with disease progression by IHC

assay (Fig. 1B). According to the semi-quantitative scoring (Ishak score) of human liver specimens, we found a positive correlation between ASCT2 expression and the F stage of patients (Fig. 1C, $r = 0.9498$, $P < 0.0001$). We next investigated the expression profile of ASCT2 in two well-established experimental liver fibrosis models, CCl_4 and bile duct ligation (BDL). H&E staining, Masson staining and α-SMA IHC showed the typical fibrosis occurred in mice livers (Fig. 1D). In addition, up-regulated ASCT2 were observed in the fibrotic bridging area of liver fibrosis mice by IHC (Fig. 1E). ASCT2 expression significantly

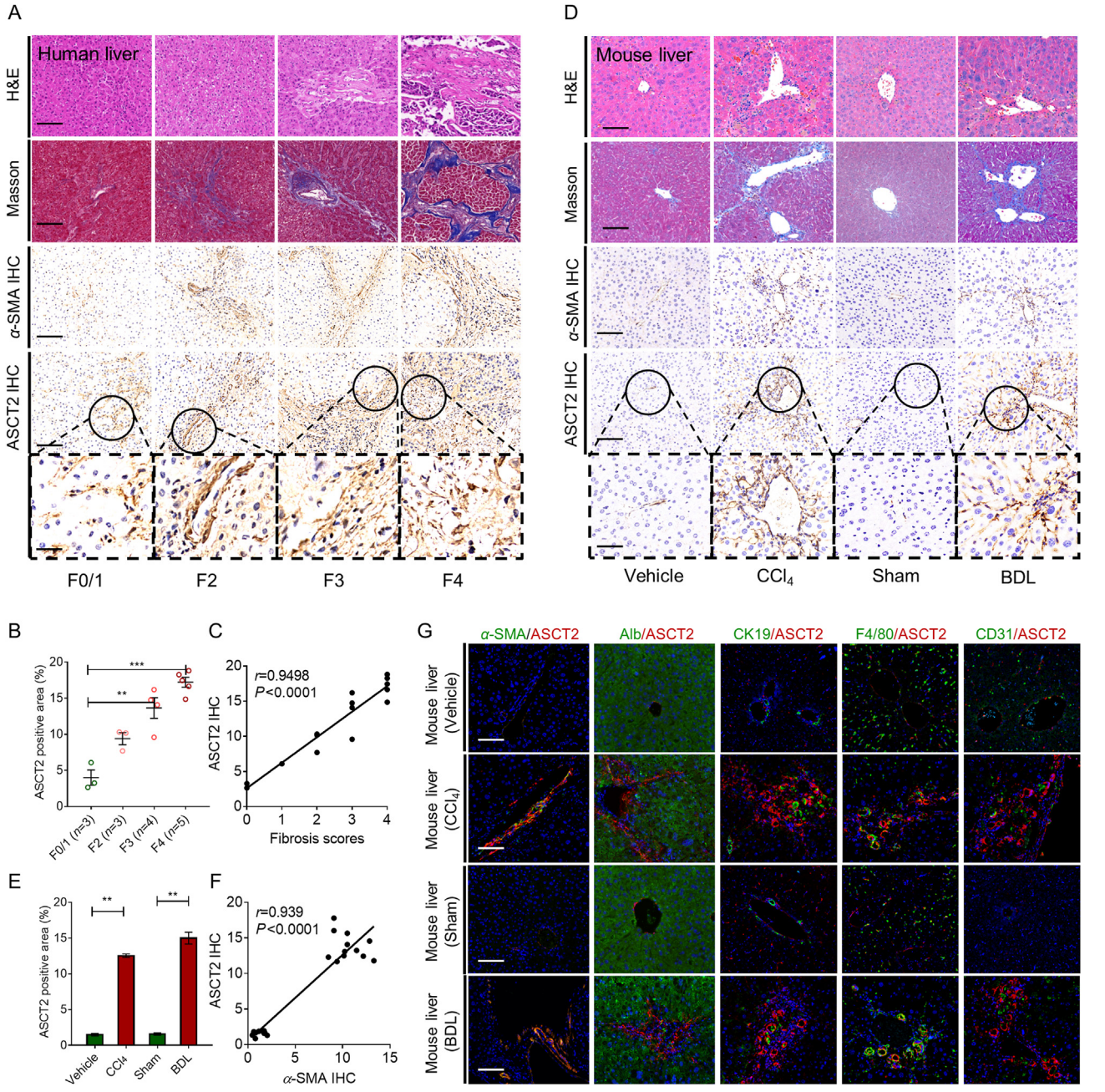

Figure 1 Enhanced ASCT2 in HSCs correlate with the progression of liver fibrosis. (A) The liver fibrosis stage was assessed by Ishak scale. For histopathological study, 15 human liver samples (F0/1, 3; F2, 3; F3, 4; F4, 5) were stained with H&E Masson and IHC for α-SMA and ASCT2. Representative images were shown. Scale bar: 50 μm, 20 μm (boxes), $n = 6$ per group. (B) The quantification of positive ASCT2 IHC ($n = 6$ per group). $^{**}P < 0.01$; $^{***}P < 0.001$. (C) Correlation analysis between ASCT2 IHC and fibrosis scores in fibrotic human livers. Spearman's correlation coefficients (r), P values are indicated. (D) Representative images of H&E and Masson staining and IHC for α-SMA and ASCT2 in mice liver fibrosis models of CCl_4 and BDL. Scale bar: 50 μm, 20 μm (boxes), $n = 6$ per group. (E) The quantification of positive ASCT2 IHC ($n = 6$ per group). $^{**}P < 0.01$. (F) Correlation analysis between ASCT2 IHC and α-SMA IHC in fibrotic human livers. Spearman's correlation coefficients (r), P values are indicated. (G) Representative immunohistofluorescence photographs for co-staining of ASCT2 (red) with α-SMA (green), Alb (green), CK19 (green), F4/80 (green) and CD31 (green) in the hepatic lobule of mice livers. Nuclei were counterstained with DAPI. Scale bar: 50 μm, $n = 6$ per group. Bars indicate mean ± SEM.

positive correlated with α-SMA expression in the experimental liver fibrosis models (Fig. 1F, $r = 0.9498$, $P < 0.0001$). In fibrotic tissues, we noticed that ASCT2 was mainly localized in fibrotic septa. To characterize the main cell types expressing ASCT2 in fibrosis, we co-stained ASCT2 with specific hepatic parenchymal cell markers: Albumin for hepatocytes (HEPs) and cytokeratin 19 for bile duct epithelium; and non-parenchymal cell markers: CD31 for liver sinusoidal endothelial cells (LSECs), F4/80 for Kupffer cells (KCs) and α-SMA for activated HSCs in mouse fibrotic liver tissues. We found that ASCT2 expression was largely co-localized with α-SMA in activated HSCs (Fig. 1G). Taken together, these data demonstrate that the enhanced ASCT2 originated from activated HSCs during liver fibrosis.

3.2. *ASCT2 knockdown ameliorates experimental liver fibrosis*

To further evidence the role of ASCT2 in liver fibrosis, we used adeno-associated virus (AAV)-shASCT2 to treat CCl_4-induced mice fibrosis model (Fig. 2A). Because AAV vectors are already used for liver-directed human gene therapy and showed the potency for a therapy of liver fibrosis[35]. Herein, histological examination, hydroxyproline (Hyp) content, α-SMA IHC and serum analyses indicated that the degree of fibrosis was alleviated upon AAV8-shASCT2 treatment (Fig. 2B−D, Supporting Information Fig. S1). Besides, we found that ASCT2 expression is downregulated, as expected (Fig. 2E). Because whether AAV8-shASCT2 transduced to HSCs was unknown, we isolated the different cell types (primary HSCs, KCs and HEPs) from mouse livers. We found the expression of ASCT2 is upregulated in activated HSCs in fibrosis, and ASCT2 knockdown markedly decreased ASCT2 expression, but did not altered in KCs and HEPs (Fig. 2F and G). Moreover, decreased glutamine and ATP levels were demonstrated in ASCT2 knockdown-fibrotic livers, as well as decreased α-KG and ATP levels in isolated HSCs, but not in isolated HEPs and KCs from mice (Supporting Information Fig. S2). Besides, the efficacy and selectivity of the knockdown were verified by decreased ASCT2 expression in activated HSCs, as shown by immunofluorescence (Fig. 2H).

Furthermore, quantitative real-time PCR (qPCR) analysis in primary HSCs demonstrated that ASCT2 knockdown markedly suppressed mRNA levels of HSC activation markers, ACTA2, COL1A1, PDGFA and PDGFRB. And showed an induction of quiescent HSC markers genes GFAP and LRAT upon ASCT2 knockdown (Fig. 2I). These results were consistent with Western blotting, which concluded that ASCT2 knockdown inhibited HSCs activation and triggered the deactivation of HSCs (Fig. 2J). We then inhibited ASCT2 using siRNA or Benser (an inhibitor of ASCT2) in rat HSC-T6 and human HSC-LX2 cells. Inhibition of ASCT2 in HSC-LX2 and HSC-T6 cells decreased both mRNA and protein of α-SMA and COL1α1 (Supporting Information Fig. S3). Taken together, we demonstrate that the inhibition of ASCT2 induces deactivation of HSCs and thus ameliorates liver fibrosis.

3.3. *ASCT2 inhibition induces activated HSCs to senescence*

We hypothesized that ASCT2 could be involved in HSC senescence. We observed ASCT2-inhibition HSC-LX2 and HSC-T6 cells entered quiescence *via* negative incorporation of EdU (Fig. 3A−D). We also found a significant increase of SA-β-Gal^+ cells in ASCT2-inhibited HSCs *via* SA-β-Gal staining (Fig. 3E and F). In addition, ASCT2 inhibition increased the expression of $p16^{INK4a}$ and $p21^{CIP1}$, two senescence markers (Fig. 3G). Cell cycle arrest is the most critical feature of senescence, and cell cycle progression is the result of interactions between cyclins and their cyclin-dependent kinases (CDKs)[15]. Here, ASCT2 inhibition slowed the G0/G1 phase checkpoints evidenced by downregulation of Cyclin D1/CDK4 complex and Cyclin E1/CDK6 complex (Fig. 3H). We further observed intuitive G0/G1 cell cycle arrest in ASCT2 inhibited-HSCs by flow cytometry (Fig. 3I). Together, these results reveal that inhibition of ASCT2 stimulated activated HSCs to senescence.

As ASCT2 is an acronym standing for alanine-serine-cysteine transporter 2. However, this historical name revealed misleading because the preferred substrate that underlies the main physiological functions of ASCT2 is glutamine. Here, we supplied the amino acids with L-glutamine, L-serine, L-asparagine, L-threonine to analyze the charging state of HSCs senescence upon ASCT2 inhibition. We observed a profound unchanging of positive SA-β-Gal^+ cells in L-serine, L-asparagine, L-threonine-treated but not L-glutamine-treated HSCs after ASCT2 depletion (Supporting Information Fig. S4A). Further upregulation of senescence markers $p16^{INK4a}$ and $p21^{CIP1}$ (Fig. S4B), and downregulation of Cyclin D1/CDK4 complex and Cyclin E1/CDK6 complex in L-serine, L-asparagine, L-threonine-treated but not L-glutamine-treated HSCs after ASCT2 depletion were showed (Fig. S4C). These data suggest that an ability to transport glutamine by ASCT2 could lead to activated HSCs to senescence.

3.4. *ASCT2 inhibition restricts the proinflammatory SASP in senescent HSCs*

To test the correlation of ASCT2 inhibition with the *SASP*, we exposed LX2 cells to the chemotherapeutics agent-etoposide, which induce growth arrest and high SASP production[36]. The RNA-seq data revealed that etoposide-treated senescent HSCs showed the enlarged proinflammatory *SASP* genes. Surprisingly, a not altered proinflammatory *SASP* was displayed in ASCT2-depleted senescent HSCs, which implied that ASCT2 inhibition had a unique proinflammatory SASP manifest in senescent HSCs (Fig. 4A). Besides, Gene set enrichment analysis (GSEA) showed that gene ontology terms associated with biological processes, such as “glutamine metabolism, TCA cycle” and “DNA replication, G1 checkpoint” were depressed under ASCT2 depletion (Fig. 4B and C). Subsequently qPCR confirmed ASCT2 inhibition induced SASP including increase of anti-inflammatory such as IL10 and TNFA, but lacks the proinflammatory SASP such as IL1A, IL1B, IL6, and IL8 (Fig. 4D and E).

To better understand the inhibitory effects of ASCT2 on SASP, we simultaneously used 4-hydroxytamoxifen (4-OHT) to induce SASP in senescent cells[37]. Senescent LX2 cells were cultured in the absence or presence of 4-OHT, and there is a stable senescence-associated growth arrest identified by increased SA-β-Gal activity (Fig. 4F), reduced EdU incorporation (Fig. 4G), and G0/G1 cell cycle arrest (Fig. 4H). However, 4-OHT elevated IL1B, IL6 and IL8 mRNA and IL-8 protein, even in ASCT2-depleted LX2 cells (Fig. 4I−L). We next determined the paracrine effects of the proinflammatory SASP on surrounding HSC migration, which was related to the microenvironments within the space of Disse in liver fibrosis[38]. Conditioned medium (CM) were collected from senescent cells to culture activated HSCs (Supporting Information Fig. S5A and S5B). In this setting, we performed the cellular migration assays and matrix degradation detection, and we found that CM from etoposide-exposed

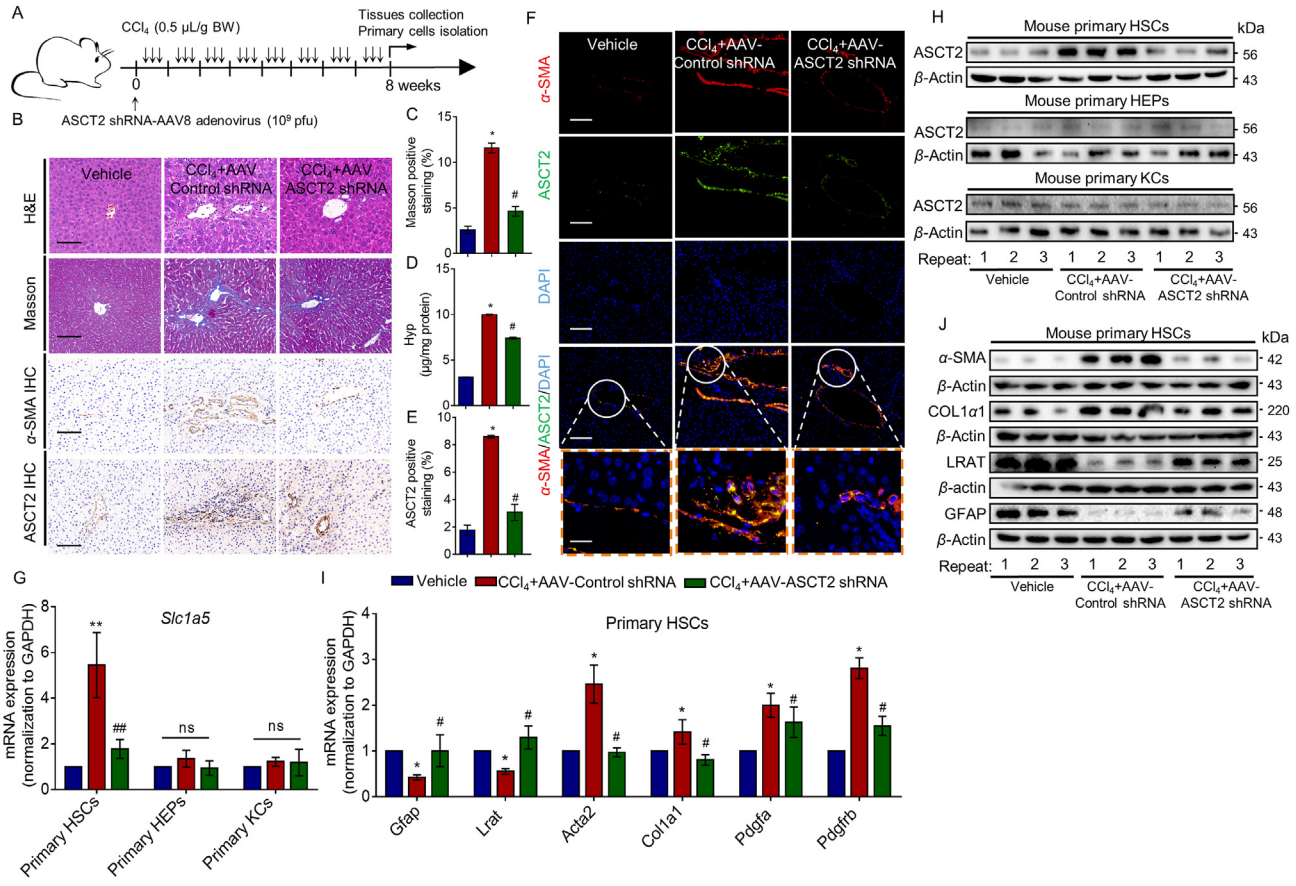

Figure 2 ASCT2 knockdown ameliorates experimental liver fibrosis. (A) AAV8 adenovirus delivery-ASCT2 shRNA and AAV8 adenovirus scramble were treated into CCl_4-induce liver fibrosis mice. (B) For histopathological study, mice liver sections were stained with H&E and Masson. And representative images of IHC for ASCT2 and α-SMA in mice fibrotic liver sections were shown. Scale bar: 50 μm, $n = 6$ per group. (C) The quantification of positive masson staining. (D) Determination of Hyp in mice liver sections. (E) The quantification of positive ASCT2 IHC was measured. (C)−(E): $n = 6$ per group; $^{*}P < 0.05$ *vs.* vehicle mice; $^{\#}P < 0.05$ *vs.* CCl_4 mice. (F) IHF for co-staining of ASCT2 (green) and α-SMA (red) in the hepatic lobule of mice livers. Nuclei were counterstained with DAPI. Scale bar: 50 μm, 20 μm (boxes), $n = 6$ per group. (G) mRNA level of ASCT2 was determined in isolated primary HSCs, KCs and HEPs by real-time PCR ($n = 5$ per group). $^{**}P < 0.01$ *vs.* vehicle mice; $^{\#\#}P < 0.01$ *vs.* CCl_4 mice. (H) protein of ASCT2 was determined in isolated primary HSCs, KCs and HEPs by Western blot ($n = 3$ per group). (I) mRNAs of HSC activation markers ACTA2, COL1A1, PDGFA and PDGFRB, and quiescent HSC markers GFAP and LRAT were determined in indicated mouse primary HSCs by qPCR ($n = 5$ per group). $^{*}P < 0.05$ *vs.* vehicle mice; $^{\#}P < 0.05$ *vs.* CCl_4 mice. (J) protein of HSC activation markers α-SMA, COL1α1, PDGF and PDGFRβ, and quiescent HSC markers GFAP and LRAT were determined in indicated mouse primary HSCs by Western blot ($n = 3$ per group). Bars indicate the mean ± SEM. ns, no significance.

senescent HSCs substantially enhanced HSCs migration capacity. But CM from ASCT2 shRNA-derived senescent HSCs did not affect cellular migration, which was abolished by 4-OHT (Fig. S5C−S5H). Overall, these data collectively indicate inhibition of ASCT2 triggered HSC senescence with proinflammatory SASP less that overlapped yet differed from other senescence-inducers.

3.5. *ASCT2-mediated glutaminolysis controls the proinflammatory SASP*

Because we found ASCT2 is required for proinflammatory SASP. As known of effect of ASCT2 in glutaminolysis, we profiled the steady-state metabolites under ASCT2 inhibition or ASCT2 overexpression (Fig. 5A). Consistently, the decreased glutamine level (the direct ASCT2 metabolite) was observed in LX2 cells upon ASCT2 inhibition. But an increase of glutamine was shown under ASCT2 overexpression (Fig. 5B). Glutamate, α-KG and GSH levels were also significantly increased by ASCT2 overexpression, but were decreased by ASCT2 inhibition in LX2 cells (Fig. 5C−E). Subsequently, we next uncovered that ASCT2 overexpression significantly increased intracellular citrate, malate, fumarate, and succinate levels (metabolites in TCA cycle), but ASCT2 inhibition decreased these metabolites levels in LX2 cells (Fig. 5F−I), accompanied with elevated intracellular ATP by ASCT2 overexpression, but reduced intracellular ATP by ASCT2 inhibition (Fig. 5J). Next, we examined the oxygen consumption rates (OCR) in ASCT2 inhibition- or ASCT2 overexpression-LX2 cells as the metabolic fitness. Importantly, ASCT2 overexpression significantly increased the mitochondrial maximal respiration capacity (OCR after FCCP injection), and mitochondria respiration was suppressed by ASCT2 inhibition (Fig. 5K), supporting the hypothesis that ASCT2 supplies metabolites and maintains mitochondrial function. We further tested the hypothesis that ASCT2-mediated glutaminolysis might correlate with the proinflammatory SASP senescent HSCs. The addition of

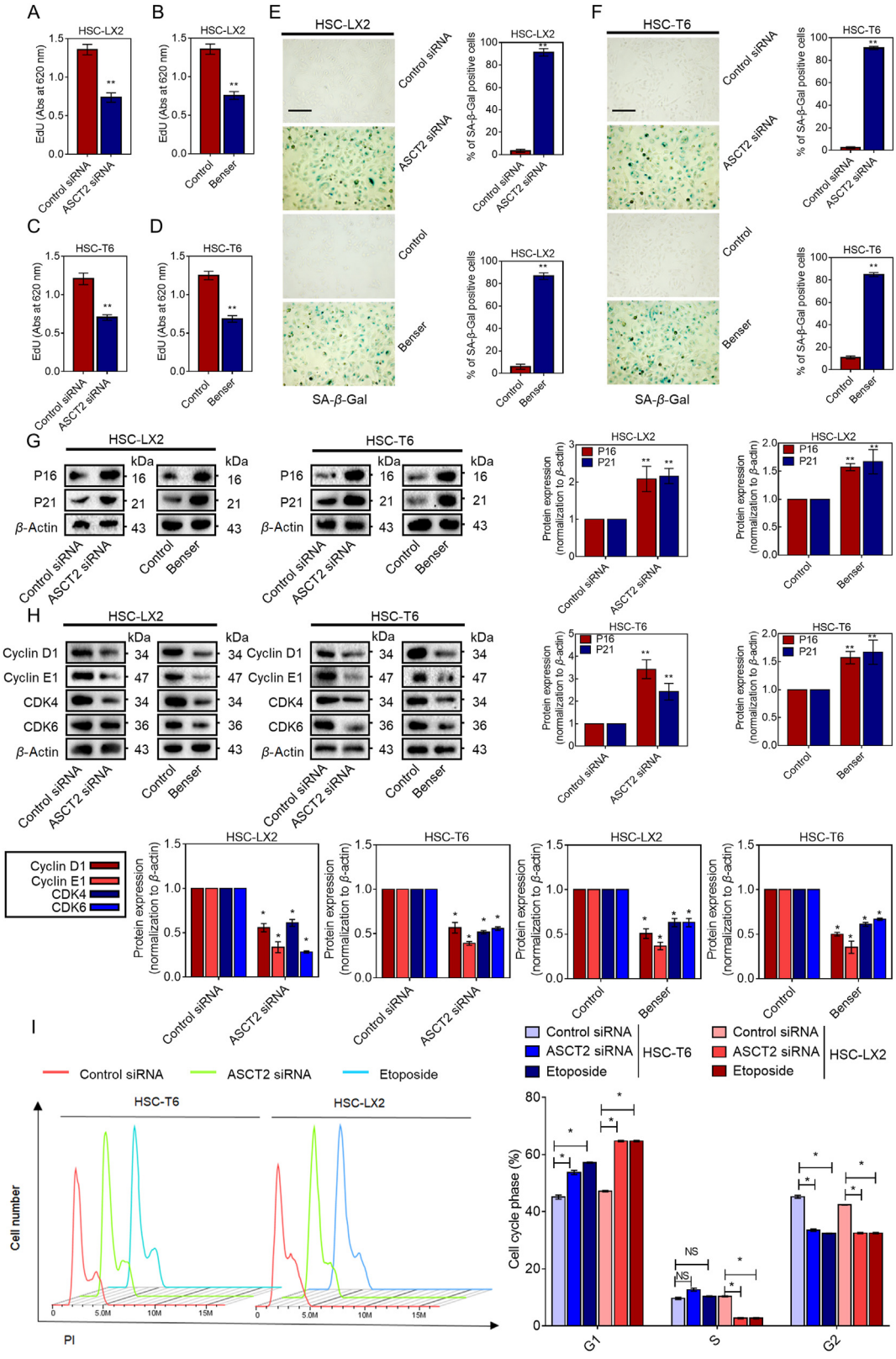

Figure 3 Inhibition of ASCT2 leads activated HSCs to senescence. (A−D) Quantitation of EdU incorporation in indicated cells at indicated treatment ($n = 8$ per group). (E, F) Representative images and the quantification of SA-β-Gal staining in the indicated cells at indicated treatment ($n = 4$ per group). Scale bar: 50 μm. (G) The indicated cells with indicated treatment were studied for the indicated proteins by Western blot ($n = 3$ per group). (H) G1 phase to S phase checkpoint protein were established by Western blot ($n = 3$ per group). (I) Cell cycle disruption was analyzed by flow cytometry ($n = 3$ per group). Bars indicate mean ± SEM; $^*P < 0.05$, $^{**}P < 0.01$.

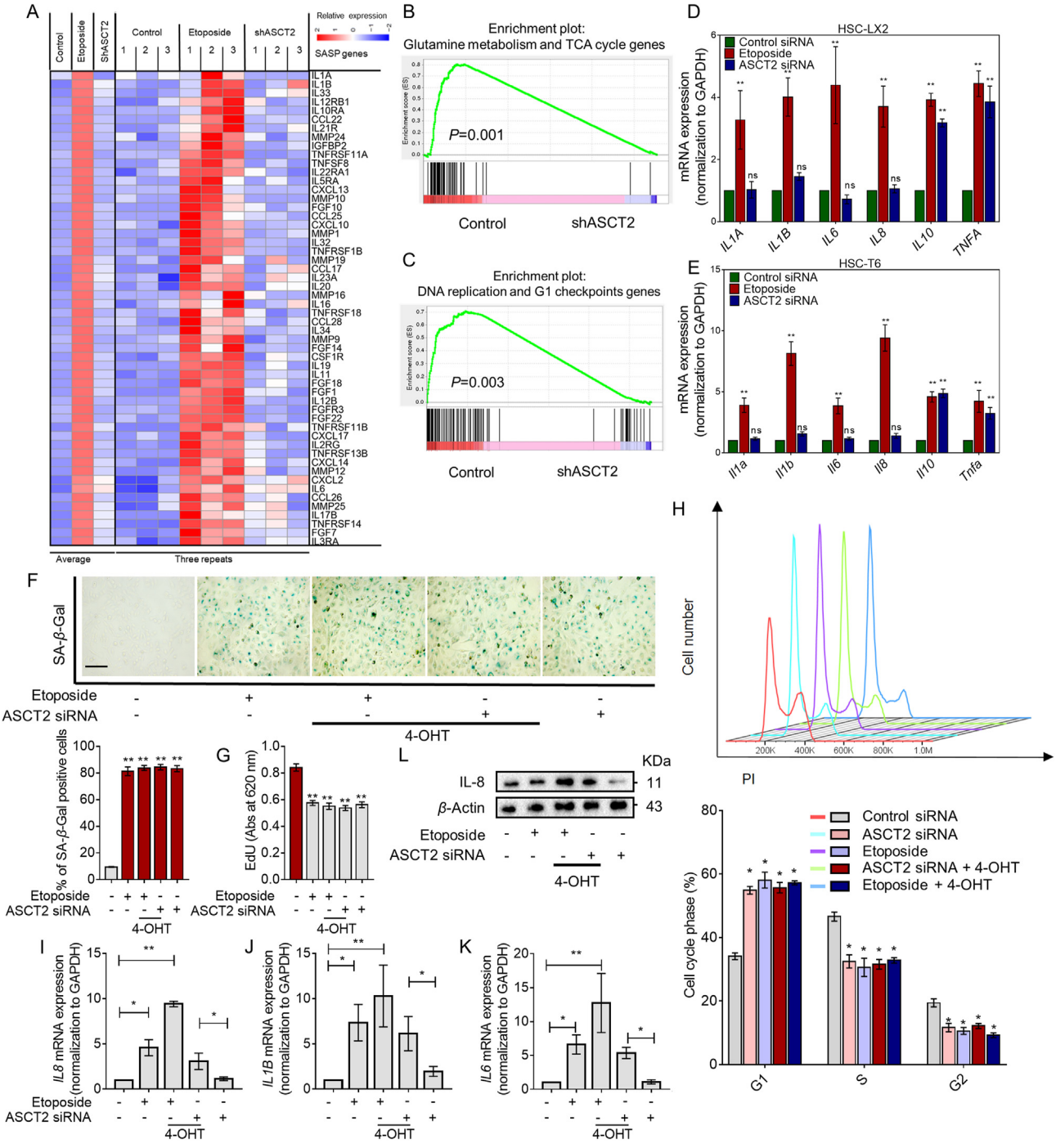

Figure 4 Inhibition of ASCT2 restricts proinflammatory SASP in senescent HSCs. (A) mRNA changes under the indicated conditions were observed by RNA-seq. Heat map indicates the fold changes of SASP factors in proliferating LX2 cells *vs.* etoposide-induced senescent LX2 cells *vs.* ASCT2 depletion-derived senescent LX2 cells. $n = 3$ per group. (B) GSEA analysis of glutamine genes and TCA cycle genes in the proliferating LX2 cells *vs.* ASCT2 depletion-derived senescent LX2 cells. (C) GSEA analysis of DNA replication genes and G1 checkpoints genes in proliferating LX2 cells *vs.* ASCT2 depletion derived-senescent LX2 cells. (D, E) mRNAs of the proinflammatory SASP: IL1A, IL1B, IL6, and IL8 were determined by qPCR in the indicated cells ($n = 3-10$ per group). (F, G) EdU incorporation and SA-β-Gal staining for senescence determination after 4-OHT stimulation ($n = 8$ per group). (H) Cell cycle distribution was determined by flow cytometry after 4-OHT stimulation ($n = 3$ per group). (I–L) mRNA levels of *IL1B*, *IL6*, and *IL8*, and protein levels of IL-8 were established by qPCR and Western blot ($n = 3-5$ per group). Bars indicate the mean ± SEM; $^*P < 0.05$, $^{**}P < 0.01$; ns, no significance.

exogenous α-KG was sufficient to restore glutaminolysis[39]. Surprisingly, the supplementation with DM-α-KG restored the proinflammatory SASPless (IL1A, IL1B, IL6, and IL8) upon ASCT2 inhibition (Fig. 5L–O). Together, these results suggest that the proinflammatory SASP in senescent HSCs were regulated by ASCT2-mediated glutaminolysis.

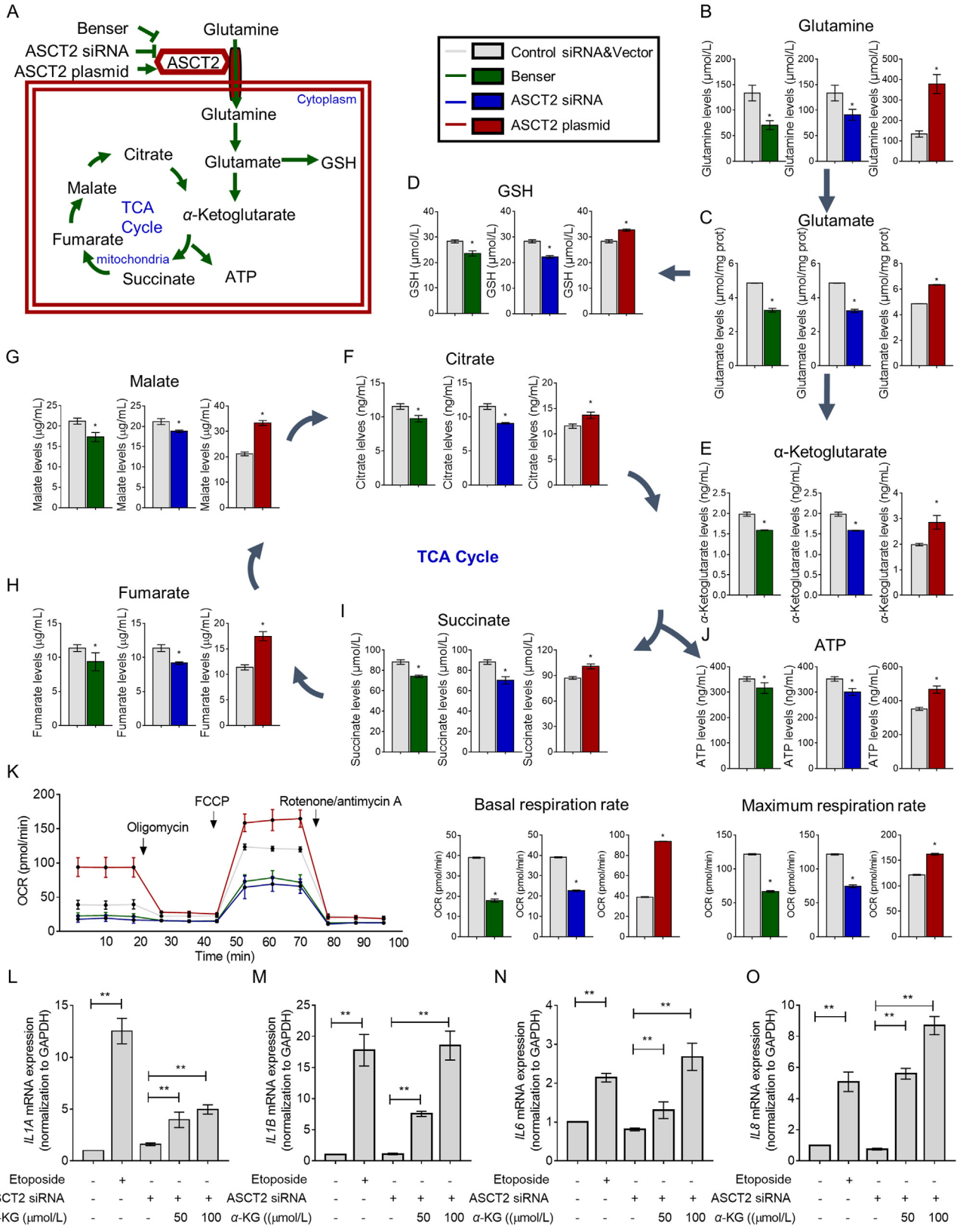

Figure 5 ASCT2-mediated glutaminolysis governs the proinflammatory SASP of senescent HSCs. (A) Schematic diagram of glutaminolysis. (B−E) Steady-state metabolite levels of glutamate, α-KG and GSH levels were measured using kits (n = 3−15 per group). (F−I) TCA cycle metabolites citrate, malate, fumarate and succinate levels were measured using kits (n = 5 per group). (J) Intracellular ATP production was determined using a kit (n = 6 per group). (K) OCR was determined and the basal respiratory rate and maximum respiration rate were quantified by seahorse assay (n = 3 per group). (L−O) mRNA levels of the proinflammatory SASP factors *IL1A*, *IL1B*, *IL6*, and *IL8* were measured by real-time PCR after α-KG supplementation (n = 5 per group). Bars indicate mean ± SEM; $^{*}P < 0.05$; $^{**}P < 0.01$.

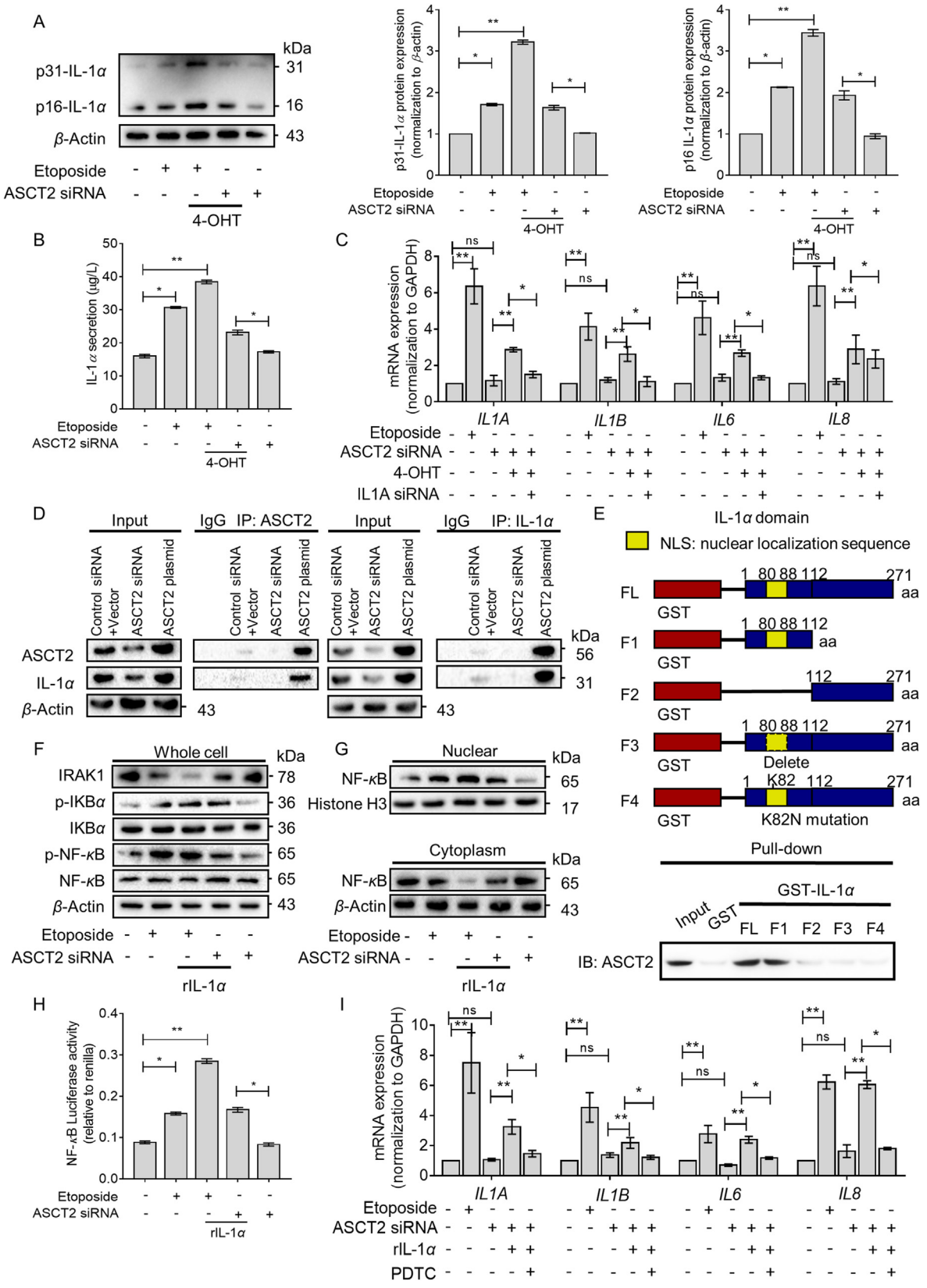

Figure 6 ASCT2 drives the proinflammatory SASP *via* IL-1α/NF-κB feedback loop through interacting with precursor IL-1α at Lys82 of senescent HSCs. (A) Protein of p31−IL-1α and p16−IL-1α was measured by Western blot analysis with 4-OHT ($n = 3$ per group). (B) Detection of intracellular IL-1α by ELISA with 4-OHT ($n = 3$ per group). (C) mRNAs of proinflammatory SASP including *IL1A*, *IL1B*, *IL6* and *IL8* were measured by qPCR ($n = 5$ per group). (D) Co-IP of ASCT2 with IL-1α in LX2 cells, as detected by Western blot analysis ($n = 3$ per group). (E) Schematic of fragments of IL-1α that were fused to GST (top) and were transfection into 293T cells. Binding of ASCT2 to GST-IL-1α proteins

3.6. *ASCT2 drives proinflammatory SASP through IL-1α/NF-κB feedback loop*

The regulation and induction of SASP is still unclear. Recent observations demonstrated that IL-1α has been reported as an upstream regulator of SASP[40]. We therefore measured IL-1α expression in proliferating HSCs, etoposide-treated senescent HSCs and ASCT2-depleted senescent HSCs. Silencing of ASCT2 showed IL-1α reduction compared with etoposide (Supporting Information Fig. S6A). We found 4-OHT restored IL1α level in ASCT2-depleted HSCs near to those with etoposide. Interestingly, a band of approximately 16 kDa band of IL-1α was detected in the presence of 4-OHT (Fig. 6A). The 16 kDa amino domain contains the nuclear localization signal (NLS), located in its N-terminal propiece, and represents the precursor IL-1α (pIL-1α) form[41]. So far, it remains a matter whether pIL-1α is necessary for efficient IL-1α-dependent biological responses. Here, we found the increased abundance of secreted IL-1α on the senescent HSCs surface (Fig. S6B), which was counteracted by 4-OHT, as expected (Fig. 6B). Further, addition of 4-OHT enhanced the SASP was suppressed by siRNA-mediated IL1α depletion in senescent cells (Fig. 6C). We postulated that pIL-1α might be a critical target for ASCT2. And we found ASCT2/IL-1α interaction by co-immunoprecipitation (co-IP) (Fig. 6D). Since the observation implied that ASCT2 had the impact on pIL-1α, we thus mapped the domains of pIL-1α into 293T cells. In GST pull down assay, ASCT2 directly interacted with IL-1α through the NLS domain containing lysine 82 (Fig. 6E). IL-1α binds its receptor (IL1R1) and activates a signaling cascade that leads to nuclear translocation of NF-κB[40]. We tested the possibility that phosphorylated IκBα and phosphorylated NF-κB were reduced by ASCT2 depletion compared with etoposide, which indicated the regulation on IL1R1 signaling by ASCT2 (Fig. S6C). Subsequently, NF-κB translocation to the nucleus was inhibited upon ASCT2 depletion (Fig. S6D). Corroborating with this idea, LX2 cells were grown in the absence or presence of recombinant IL-1α (rIL-1α), and the increased SA-β-Gal activity, reduced EdU incorporation and arrested cell cycle at G0/G1 (senescence phenotypes) were demonstrated (Fig. S7A−S7C), suggesting the stable senescence with rIL-1α. Importantly, rIL-1α could elevated IL1A, IL1B, IL6 and IL8 mRNAs and IL-8 protein, regardless of ASCT2-depleted LX2 cells (Fig. S7D−S7G). Further support evidenced that IL-1α-dependent proinflammatory SASP is not required for cell cycle exit, and the IL-1α/NF-κB signaling disruption uncouples the proinflammatory SASP from senescence.

We also analyzed IL-1α/NF-κB signaling in senescent HSCs upon rIL-1α addition, and found ASCT2 depletion plus rIL-1α expressed an enhanced IL-1α/NF-κB signaling (Fig. 6F). Besides, the inhibition effect of ASCT2 depletion on NF-κB translocation was rescued by the addition of rIL-1α (Fig. 6G). An NF-κB reporter assay showed that etoposide increased NF-κB activity, as reported, but failed to do so in ASCT2-depletion senescent HSCs without rIL-1α (Fig. 6H). As NF-κB stimulates the transcription of proinflammatory *SASP* genes including IL-1α[42], which indicated that there exists a positive feedback loop of IL-1α/NF-κB. To further test this idea, we used NF-κB inhibitor (PDTC) to senescent HSCs cultured with rIL-1α. PDTC reduced the elevated IL1A, IL1B, IL6 and IL8 mRNAs upon rIL-1α addition (Fig. 6I), implicating the effect of ASCT2 depletion on IL-1α/NF-κB feedback loop. Collectively, these findings suggest ASCT2 interacted with precursor IL-1α at Lysine82 for interfering IL-1α/NF-κB feedback loop, which was required for the production of proinflammatory SASP in senescent HSCs.

3.7. *Atractylenolide III direly targeting to ASCT2 through its hydroxyl group*

Atractylenolide III, a sesquiterpenoid compound, originally separated from the rhizome of atractylodisatractylodis. To date, the biological effects of atractylenolide III is largely unclear. Evidence showed that atractylenolide III is effective in treating pulmonary fibrosis and renal fibrosis[43,44]. Herein, an *in silico* homology model of ASCT2 (hASCT2) (PDB: 6GCT) was utilized for molecular docking and demonstrated atractylenolide III binds with ASCT2 in the fitting pocket contain Asn190, Asn230 and Ser203 amino acid residues (Fig. 7A and Supporting Information Fig. S8A). To identify the activity of atractylenolide III on ASCT2, HSCs were treated with atractylenolide III in dose-dependent manner, and atractylenolide III was found to be able to inhibit ASCT2 expression (Fig. 7B). The direct interaction between atractylenolide III and ASCT2 was further verified by temperature-dependent cellular thermal shift assay (Fig. 7C). Besides, in atractylenolide III-treated HSCs, LX2 cells viability was inhibited in a dose-dependent manner without cell cytotoxicity (Fig. S8B and S8C). In atractylenolide III-treated LO2, atractylenolide III did not show an inhibitory effect range to 100 μmol/L (Fig. S8D). Next, we found that atractylenolide III repressed HSC activation (Fig. S8E). Those results indicate that atractylenolide III is a promising lead compound as ASCT2 inhibitor.

Based on the docking prediction, the −OH group of atractylenolide III was found to form a hydrophobic bonding interaction to ASCT2 residue Asn230 with an 83% distribution, suggesting it is a key structural feature to bind with ASCT2 (Fig. 7D). Therefore, HSCs were treated with atractylenolide I or atractylenolide II, which differ in the number and position of −OH groups, and examined for their effects on ASCT2 expression. At both tested concentrations, atractylenolide III with an −OH group inhibited ASCT2 protein, but those without an −OH group did not show any act on ASCT2 (Fig. 7E). As for the function of ASCT2, we found atractylenolide III effectively lowered glutamine, glutamate, α-KG, and GSH levels, and reduced intracellular ATP in LX2 cells (Fig. 7F). Taken together, these results indicate that the presence of −OH groups of atractylenolide III was required for direly targeting to ASCT2 and further inhibit ASCT2.

was detected by Western blot (bottom, $n = 3$ per group). FL: full length; F1: domain 1−112; F2: domain 112−271; F3: NLS domain (80−88) deletion; F4: K82N mutation. (F) rIL-1α protein was added to senescent (ASCT2 depletion or etoposide treatment) LX2 cells, and IL1R1 signaling cascade indicators were analyzed by Western blotting ($n = 3$ per group). (G) rIL-1α protein was added to senescent (ASCT2 depletion or etoposide treatment) LX2 cells, and NF-κB protein was measured in nuclear and cytoplasmic lysates by Western blot ($n = 3$ per group). (H) Relative luciferase measurement of NF-κB in indicated cells ($n = 5$−6 per group). (I) ASCT2 depletion-senescent LX2 cells were treated with rIL-1α protein and addressed in NF-κB inhibitor PDTC, and the analysis of mRNAs of proinflammatory SASP *IL1A*, *IL1B*, *IL6* and *IL8* by qPCR ($n = 5$−6 per group). Bars indicate mean ± SEM; $^*P < 0.05$, $^{**}P < 0.01$; ns, no significance.

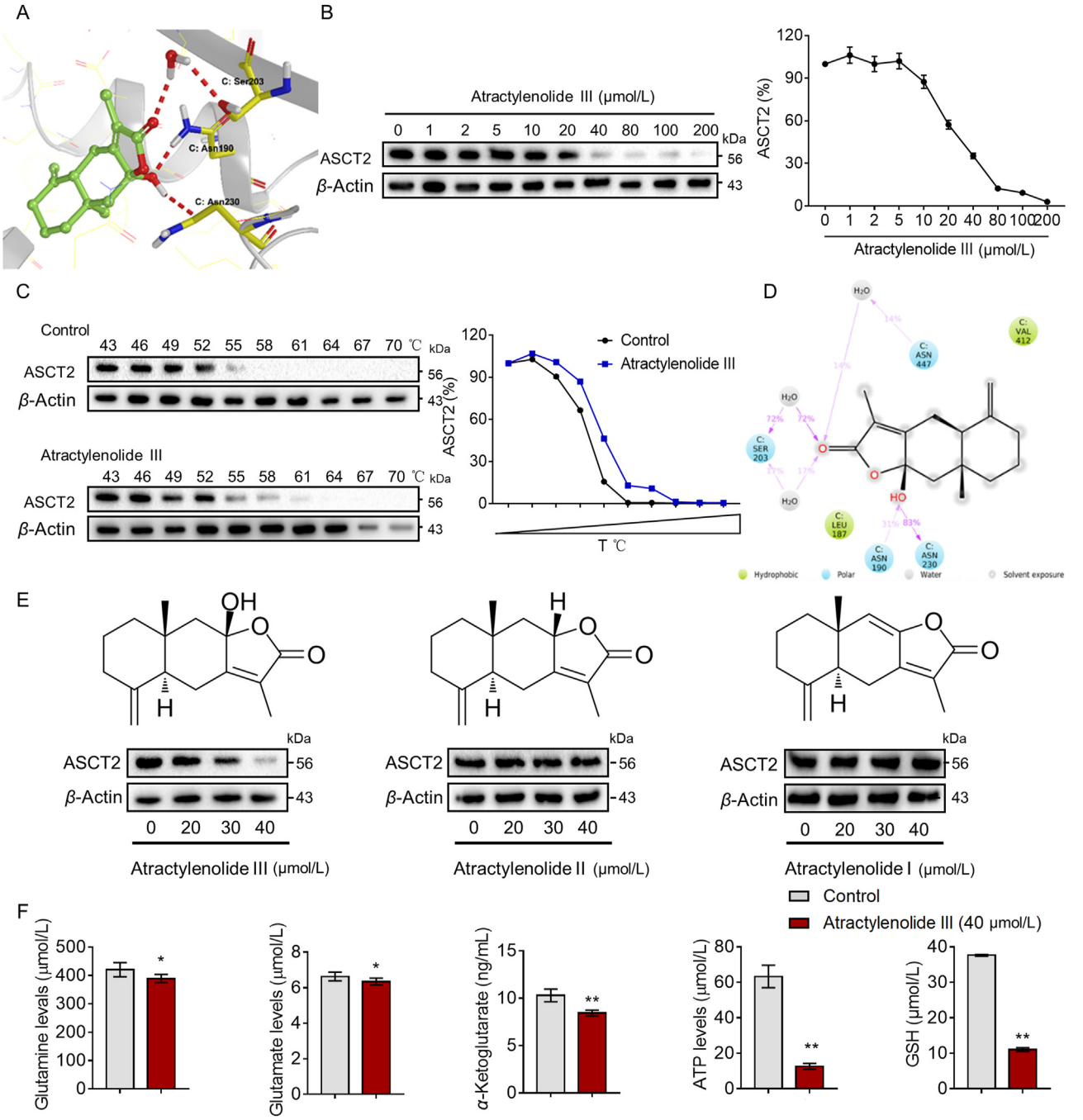

Figure 7 Atractylenolide III direly targeting to ASCT2 through its hydroxyl group. (A) Expanded view of residues proximal to atractylenolide III within the binding site. The highest scoring pose was shown. (B) Protein expression of ASCT2 in atractylenolide III concentration gradient-treated HSC-LX2 cells by Western blot. (C) HSC-LX2 cells were incubated with or without atractylenolide III (40 μmol/L) for 2 h, then the cells were collected and subjected to temperature-dependent CETSA assay of ASCT2. (D) Interaction pattern and probability distribution of binding sites of ASCT2 for atractylenolide III. (E) Chemical structures of the structurally-related atractylenolide III, atractylenolide II, atractylenolide I. And protein expression of ASCT2 was assessed in the chemical-treated HSC-LX2 cells by Western blot. (F) Intracellular glutamine, glutamate, α-KG, GSH and ATP levels were evaluated by kits in atractylenolide III-treated HSC-LX2 cells. Bars indicate mean ± SEM, $n = 3-10$ per group; $^{*}P < 0.05$; $^{**}P < 0.01$.

3.8. Asn230 of ASCT2 is required for its interaction with atractylenolide III

Our above results implied that atractylenolide III could be a potent inhibitor of ASCT2. To clarify the relationship between ASCT2 expression and the ability of atractylenolide III to HSCs senescence, HSCs were treated with atractylenolide III and the senescence assays were examined. Atractylenolide III triggered HSCs to senescence identified by high SA-β-Gal activity, low EdU labeling, up-regulated p16 and p21 protein expression

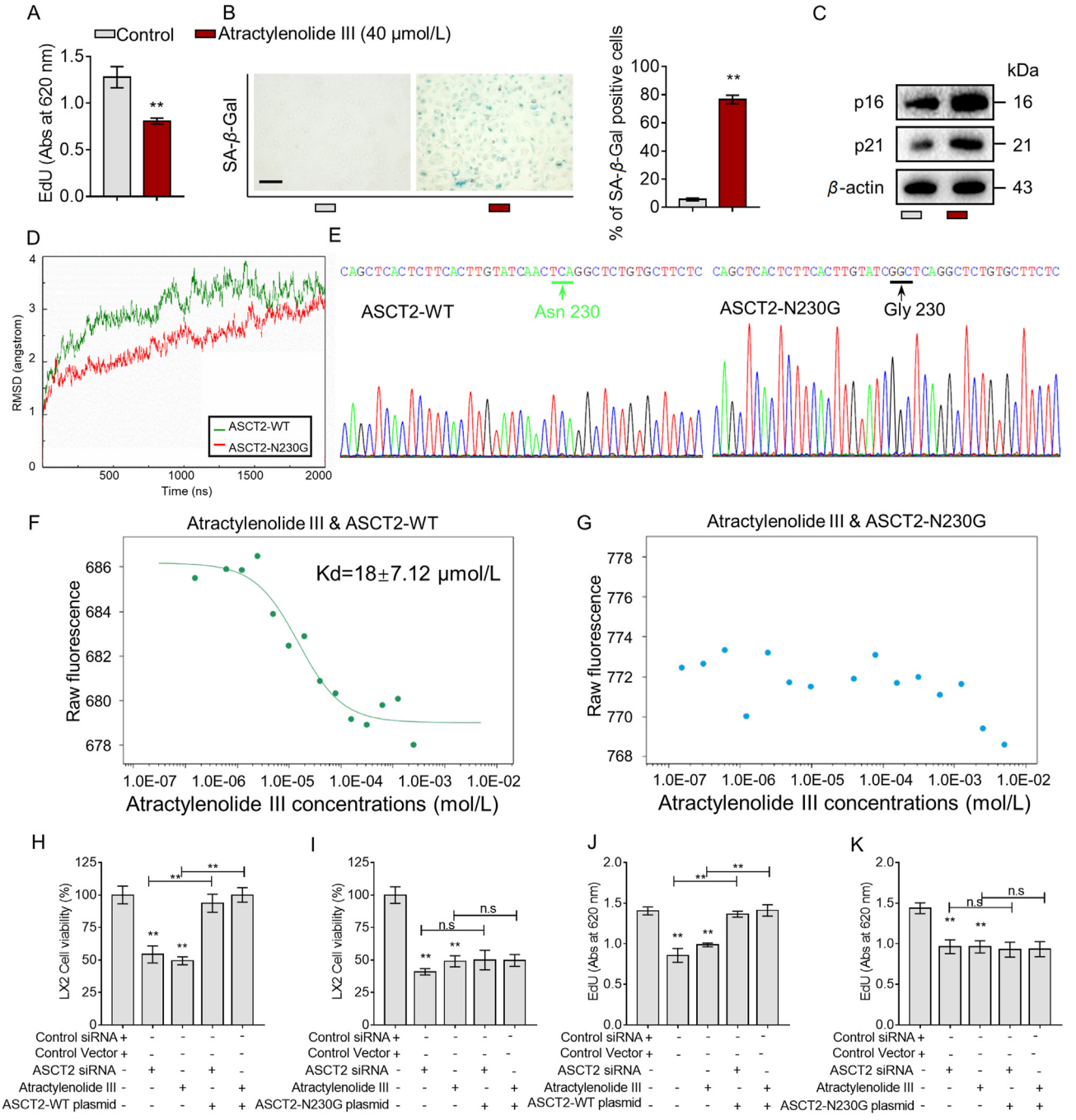

Figure 8 Asn230 of ASCT2 is required for its interaction with atractylenolide III. (A) Determination of incorporating EdU by fluorescence microplate reader (n = 6−7 per group). (B) Representative positive images and quantification of SA-β-Gal staining (n = 3 per group). Scale bar = 50 μm. (C) HSC-LX2 cells with indicated treatment were studied for the indicated proteins by Western blot. (D) The time evolution of RMSD values for ASCT2 protein and mutation protein, ASCT2-WT (green) and ASCT2-N230G (red). (E) Sequences of ASCT2-WT and ASCT2-N230G were validated. (F) Microscale thermophoresis assay (MST) for bind affinity of atractylenolide III to purified protein ASCT2-WT (n = 4 per group). (G) MST assay for bind affinity of atractylenolide III to purified protein ASCT2-N230G (n = 3 per group). (H, I) EdU incorporated was tested in re-expression ASCT2-WT or ASCT2-N230G into atractylenolide III-treatment LX2 cells (n = 8 per group). (J, K) Cell viability was tested in re-expression ASCT2-WT or ASCT2-N230G into atractylenolide III-treatment LX2 cells (n = 8 per group). Bars indicate mean ± SEM; $^{**}P < 0.01$; ns, no significance.

(Fig. 8A−C), arrested G0/G1 cell cycle and down-regulated G1 checkpoint protein in atractylenolide III treated HSCs (Supporting Information Fig. S9A and S9B). Further test of the constantly IL1A, IL1B, IL6 and IL8 mRNAs confirmed that atractylenolide III induced HSC senescence but failed to produce SASP (Fig. S9C).

The subsequent dynamic stability result showed that mutation of Asn230 changed the root mean square fluctuation (RMSF) values (Fig. 8D). Guided by these observations, we mutated Asn230 of ASCT2 to Gly (Fig. 8E), and performed microscale thermophoresis (MST) assay to investigate a direct atractylenolide III-ASCT2 binding. In our study, atractylenolide III bound to ASCT2-WT

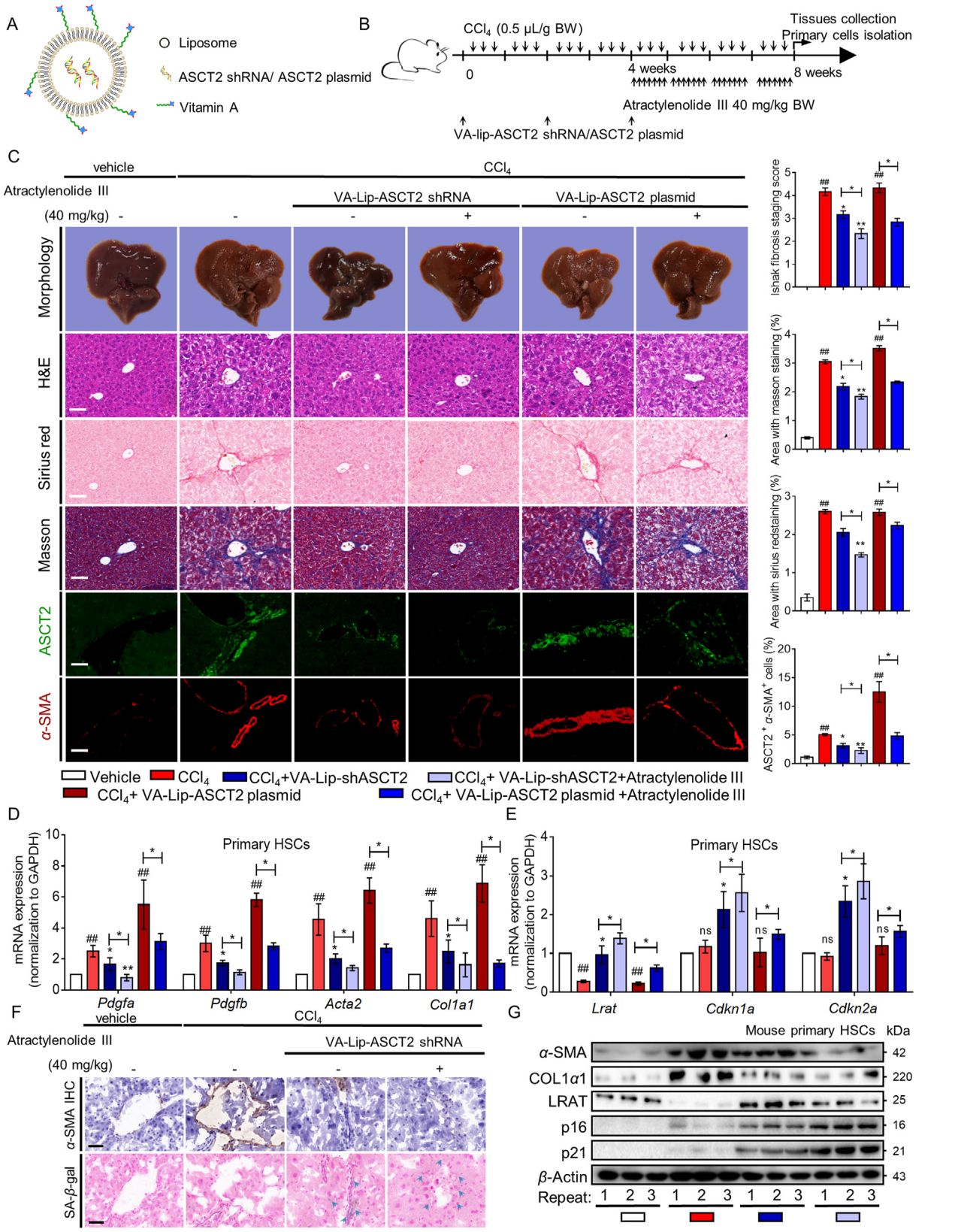

Figure 9 HSC-specific knockdown of ASCT2 elicits HSC senescence in mice liver fibrosis. 6 groups mice: vehicle, CCl_4, CCl_4+VA-Lip-ASCT2-shRNA, CCl_4+VA-Lip-ASCT2-shRNA + atractylenolide III 40 mg/kg, CCl_4+VA-Lip-ASCT2-plasmid, CCl_4+VA-Lip-ASCT2-plasmid + atractylenolide III 40 mg/kg. (A) Generation of VA-Lip-ASCT2-shRNA and VA-Lip-ASCT2-plasmid. (B) Experimental set-up of mice. (C) Pathological changes in livers were observed by macroscopic examination. Scale bar: 1 cm. For histopathological study, 4 μm liver sections were stained with H&E, Sirius red, and Masson, Scale bar: 50 μm. IHF analyses of α-SMA (red) and ASCT2 (green) expression in livers,

protein with a dissociation constant (K_d) value of 18 μmol/L (Fig. 8F). However, ASCT2-N230G mutation protein presented almost no affinity, despite the increasing concentrations of atractylenolide III (Fig. 8G). Driven by these results, atractylenolide III targeting ASCT2 through Asn230. Since the findings of atractylenolide III on ASCT2 inhibition, we re-expressed ASCT2-WT and ASCT2-N230G in atractylenolide III treated HSCs. We found the growth arrest and decreased cell viability were rescued by re-expression of ASCT2-WT, but not ASCT2-N230G (Fig. 8H−K). Collectively, Asn230 of ASCT2 is required for its interaction with atractylenolide III to regulate HSC senescence.

3.9. *ASCT2 blockade by atractylenolide III reduces liver fibrogenesis in vivo*

To further support and extend the application of our data, we examined whether atractylenolide III reduce liver fibrogenesis. The mice were pre-established liver fibrosis by a 4-weeks CCl_4 treatment, then the mice were intraperitoneally administered with vehicle oil or atractylenolide III at 20, 30, and 40 mg/kg for another 4 weeks. The CCl_4 induction was sustained during the period (Supporting Information Fig. S10A). After that, H&E, Masson and Sirius red staining revealed the typical liver fibrosis in CCl_4-induced mice, and atractylenolide III could reduce liver fibrosis (Fig. S10B). Besides, no significant changes in body weight and spleen weight highlighted the safety atractylenolide III *in vivo* (Fig. S10C and S10D). Further serum analysis showed the reduced liver injury and antifibrotic effects of atractylenolide III *in vivo* (Fig. S10F−S10L).

As expected, we found the decreased ASCT2 positive-HSCs in fibrotic septa after atractylenolide III treatment (Supporting Information Fig. S11A). We also detected the SA-β-Gal$^+$ cells in the hepatic lobule, specifically in HSCs. And we found the increased numbers of SA-β-Gal$^+$ cells but decreased α-SMA expression in the fibrotic liver under atractylenolide III administration. Importantly, SA-β-Gal$^+$ cells co-localized with those cells with positive α-SMA and exerted a negative correlation (Fig. S11B). Meanwhile, senescence markers CDKN1A and CDKN2A mRNAs were raised by atractylenolide III, and fibrogenic markers ACTA2, COL1A1, PDGFA and PDGFRB were suppressed by atractylenolide III (Fig. S11C). Similar results were next obtained by Western blotting assay (Fig. S11D). Notably, sizable populations of p21$^+$ and α-SMA$^+$ HSCs were present in livers, and HSCs were the dominant cell population negatively displaying IL-1α (a SASP component) under atractylenolide III administration (Supporting Information Fig. S12). Taken together, we conclude that atractylenolide III triggered HSC senescence as a therapeutic strategy for the treatment of liver fibrosis.

3.10. *HSC-specific knockdown of ASCT2 elicits HSC senescence in mouse liver fibrosis*

To determine whether the anti-fibrotic effect of atractylenolide III depends on ASCT2 inhibition, we used our previously characterized vitamin A-coupled liposomes nanoparticle to deliver ASCT2 shRNA or ASCT2 overexpression plasmid, which were used to downregulate ASCT2 or upregulate ASCT2 specifically in HSCs. Then atractylenolide III (40 mg/kg) administration was next performed (Fig. 9A and B). In this setting, histological examination indicated that ASCT2 knockdown alleviated fibrosis similar to atractylenolide III, but the anti-fibrotic effects of atractylenolide III were abolished by ASCT2 overexpression. The co-immunofluorescence of ASCT2 and α-SMA further identified ASCT2 is mainly expressed in activated HSCs (Fig. 9C). The efficacy and selectivity of ASCT2 knockdown or ASCT2 overexpression to HSCs were verified by the corresponding changes of ASCT2 mRNA and protein were showed in isolated primary HSCs, but not in HEPs and KCs (Supporting Information Fig. S13A and S13B). Consistent with our idea, similar with atractylenolide III treatment, HSC-specific ASCT2 knockdown attenuated liver Hyp level and serum biochemical parameters of ALT, AST, DBIL, HA, LN, PC-III and IV-C, whereas HSC-specific ASCT2 overexpression blunted the effect of atractylenolide III (Supporting Information Fig. S14). These results demonstrate that ASCT2 in HSCs was required for the anti-fibrotic activity of atractylenolide III.

Further, a comparable reduction of HSC activation markers (ACTA2, COL1A1, PDGFA and PDGFRB) by ASCT2 knockdown in isolated primary HSCs (Fig. 9D). And induction of quiescent HSC markers (GFAP and LRAT) and senescent HSC marker p16 were observed in isolated primary HSCs (Fig. 9E). Given the contribution of ASCT2 to HSC senescence, we found the increased SA-β-Gal$^+$ HSCs in HSC-specific ASCT2 knockdown-mice livers (Fig. 9F). Besides, the indicated change of protein expression forced that ASCT2 knockdown in HSCs can elicit HSC senescence (Fig. 9G). Then, we also found the upregulated of p21$^+$ and α-SMA$^+$ HSCs in ASCT2 knockdown-mice livers by co-immunofluorescence assay (Supporting Information Fig. S15A), which supported that ASCT2 as a key mediator of HSC senescence *in vivo*. Additionally, we found that ASCT2 knockdown expressed fewer SASP components, as evidenced by the populations IL-1α^+ and α-SMA$^+$ HSCs (Fig. S15B). Altogether, these findings verify that atractylenolide III targeting ASCT2 elicited HSC senescence, which represents an attractive therapeutic strategy for liver fibrosis.

4. Discussion

Evidence showed that promoting HSC senescence reduces fibrogenesis as a strategy for the treatment of liver fibrosis[45]. However, senescent cells often secrete a multi-faceted senescence-associated secretory phenotype (SASP)[46]. Therefore, discovery of senescence-inducing drugs is essential but remains a challenge. Here, we provide a basis of how ASCT2 drives HSC senescence phenotypes. Importantly, we offer the potential that atractylenolide III targeting ASCT2 has the therapeutic effect on liver fibrosis by eliciting HSC senescence with a modified SASP.

α-SMA, ASCT2, nuclei were counterstained with DAPI, Scale bar: 100 μm. Representative images are shown. The liver fibrosis stage was assessed by Ishak scale. The quantification of positive Masson staining and ASCT2 IHF was measured ($n = 6$ per group). (D) mRNAs of HSC activation markers *Acta2*, *Col1a1*, *Pdgfa* and *Pdgfrb* were determined in indicated mouse primary HSCs by qPCR ($n = 3$ per group). (E) mRNAs of quiescent HSC marker *Lrat*, and senescent HSC markers *Cdkn1a* and *Cdkn2a* were determined in indicated mouse primary HSCs by qPCR ($n = 3$ per group). (F) Representative images of SA-β-Gal staining and α-SMA IHC in cryosections from mouse liver sections ($n = 6$ per group). Scale bar: 25 μm. Arrowheads indicate cells with positive SA-β-Gal staining. (G) Western blot analysis of the indicated proteins in primary mouse HSCs ($n = 3$ per group). Bars indicate the mean ± SEM. $^*P < 0.05$; $^{**}P < 0.01$ *vs.* CCl_4, $^{\#}P < 0.05$; $^{\#\#}P < 0.01$ *vs.* vehicle.

ASCT2 expression has also been found to be upregulated in several cancers, including colorectal cancer[47], breast cancer[48], non-small cell lung cancer[49], and clear-cell renal cell carcinoma[50], suggesting that targeting ASCT2 could be a viable therapeutic option. In total, the protein expression of ASCT2 is consistently elevated *in vivo* in patients with advanced liver fibrosis, and in experimental mice models of liver fibrosis. The ASCT2 expression in liver was remarkably higher in F3 and F4 stage than in F0 stage patients with a positive correlation to the fibrotic stage. We further showed the producing ASCT2 in liver fibrosis, mainly in activated HSCs. With that, we firstly determined that the increased ASCT2 was linked to liver fibrosis and identified HSCs as the responsible cell type expressing ASCT2. Most importantly, we provided evidence that knockdown of ASCT2 in aHSCs induces deactivation of aHSCs and thus ameliorates liver fibrosis.

We originally found that ASCT2 inhibition triggered aHSCs to senescence, as demonstrated by increased SA-β-Gal activity, reduced EdU incorporation, G0/G1 cell cycle arrest, and the upregulated p16 and p21. Interestingly, ASCT2 depletion-senescent HSCs showed a SASP less manifestation. In contrast, a large amount of senescence-associated SASP was displayed etoposide-treated senescent HSCs. Indeed, the addition of 4-OHT identified the possibility that ASCT2 inhibition suppressed paracrine migration of senescence-associated proinflammatory SASP. A recent study discovered that nicotinamide adenine dinucleotide (NAD^+) metabolism controls proinflammatory SASP in oncogene-induced cellular senescence[21], which have the far-reaching implications for understanding proinflammatory SASP regulation. In our study, we found that ASCT2-mediated glutaminolysis governed proinflammatory SASP in senescent HSCs. And further, ASCT2 interacted with precursor IL-1α at Lys82, which controlled pro-IL-1α translocation and allowed it to be a signal as a membrane-bound cytokine to activate IL-1α/NF-κB feedback loop for proinflammatory SASP production.

Since we have established the biology of ASCT2 in HSC senescence and proinflammatory SASP. ASCT2 inhibitors seem to be a new strategy and a major need for drug discovery. Natural products and their structural analogues have historically made a major contribution to pharmacotherapy, and could open new avenues for drug discovery or repurposing. Herein, the molecular docking and CETSA assay indicated that atractylenolide III inhibited ASCT2 expression in cells. Furthermore, we found the presence of −OH groups of atractylenolide III was required for direly targeting to ASCT2 and the ASCT2 inhibition. Besides, site mutation and MST assays proved that Asn230 of ASCT2 was required for the interaction with atractylenolide III to regulate HSC senescence. Our *in vitro* studies further concluded that atractylenolide III brings HSC senescence with the modified proinflammatory SASP. Our *in vivo* studies showed that atractylenolide III elicited HSC senescence to reverse pre-established liver fibrosis. In particular, our data from nanoparticle delivery of ASCT2 knockdown or ASCT2 overexpression in HSCs strengthened the notion that targeting HSC ASCT2 by atractylenolide III is essential for inhibiting liver fibrosis *in vivo*.

Although atractylenolide III was effective in treating liver fibrosis, the effect of atractylenolide III in preventing liver fibrosis remain to be confirmed. Furthermore, it has been recognized that advanced fibrosis in human is less reversible than in rodents, likely due to the densely cross-linked and accumulated ECM over decades in patients. There are insufficient information and limited evidence of the benefits of atractylenolide III in liver fibrosis from clinical studies. Therefore, it is crucial to add more preclinical trials to further validate the role of atractylenolide III in liver fibrosis. Besides, the transcription regulatory of atractylenolide III on ASCT2 warrants a further investigation. Another issue is the duration of senescence-induced therapy for fibrosis. Senescent HSCs need to be removed to exclude unwanted long-term effects of accumulated senescent HSCs. For this reason, pro-senescence therapy like ASCT2 inhibitory might be combined with senolytics including dasatinib and quercetin (D + Q)[51] and ABT-263[52] in order to minimize the disadvantages and detrimental effects of accumulated senescent cells. However, the identification of highly specific and effective therapy of ASCT2 inhibitory combined with senolytics is still an ongoing challenge.

5. Conclusion

Our findings indicate that ASCT2 is elevated in human and mice liver fibrosis and originally from aHSCs. Inhibition of ASCT2 drove HSC senescence with a modified proinflammatory SASP *via* regulation of glutaminolysis-associated IL-1α/NF-κB feedback loop. Our findings provide a preclinical basis that atractylenolide III could be a potential lead compound to inhibit ASCT2 and have the ability to prevent fibrosis progression.

Acknowledgments

We would like to thank Dr. Shuai Lu (School of Science, China Pharmaceutical University, Nanjing, China) for his assistance in molecular docking assay. We thank Experiment Center for Science and Technology of Nanjing University of Chinese Medicine for assistance in experimental instruments. This work was financially supported by the National Natural Science Foundation of China (81870423, 82173874 and 82073914), the Major Project of the Natural Science Research of Jiangsu Higher Education Institutions (19KJA310005, China), the Open Project of Chinese Materia Medica First-Class Discipline of Nanjing University of Chinese Medicine (2020YLXK022 and 2020YLXK023, China), the Open Project of Jiangsu Key Laboratory for Pharmacology and Safety Evaluation of Chinese Materia Medica (JKLPSE202005, China), the Qing Lan Project of Jiangsu Higher Institutions (Young and Middle-Aged Academic Leader, China), and the Postgraduate Research & Practice Innovation Program of Jiangsu Province (KYCX20_1493, China).

Author contributions

Feixia Wang, Feng Zhang, and Shizhong Zheng: conceptualization, methodology, and validation. Zhanghao Li, Li Chen, Ting Yang, and Baoyu Liang: formal analysis. Hai Ding, Jiangjuan Shao, Zili Zhang, Xuefen Xu, Shijun Wang, and Guoping Yin: data curation. Feng Zhang, Shizhong Zheng, and Feixia Wang: funding acquisition. Feixia Wang: writing-original draft. Feng Zhang: writing-review & editing.

Conflicts of interest

The authors declare no conflicts of interest.

Appendix A. Supporting information

Supporting data to this article can be found online at https://doi.org/10.1016/j.apsb.2022.03.014.

References

1. Lee YA, Wallace MC, Friedman SL. Pathobiology of liver fibrosis: a translational success story. *Gut* 2015;**64**:830−41.
2. Friedman SL. Stellate cells: a moving target in hepatic fibrogenesis. *Hepatology* 2004;**40**:1041−3.
3. Kisseleva T. The origin of fibrogenic myofibroblasts in fibrotic liver. *Hepatology* 2017;**65**:1039−43.
4. Wang S, Friedman SL. Hepatic fibrosis: a convergent response to liver injury that is reversible. *J Hepatol* 2020;**73**:210−1.
5. Zhang F, Lu S, He J, Jin H, Wang F, Wu L, et al. Ligand activation of PPARgamma by ligustrazine suppresses pericyte functions of hepatic stellate cells *via* SMRT-mediated transrepression of HIF-1alpha. *Theranostics* 2018;**8**:610−26.
6. Shen M, Guo M, Wang Z, Li Y, Kong D, Shao J, et al. ROS-dependent inhibition of the PI3K/Akt/mTOR signaling is required for oroxylin A to exert anti-inflammatory activity in liver fibrosis. *Int Immunopharm* 2020;**85**:106637.
7. Wang F, Jia Y, Li M, Wang L, Shao J, Guo Q, et al. Blockade of glycolysis-dependent contraction by oroxylin a *via* inhibition of lactate dehydrogenase-a in hepatic stellate cells. *Cell Commun Signal* 2019;**17**:11.
8. Zhang F, Wang F, He J, Lian N, Wang Z, Shao J, et al. Regulation of hepatic stellate cell contraction and cirrhotic portal hypertension by Wnt/beta-catenin signalling *via* interaction with Gli1. *Br J Pharmacol* 2021;**178**:2246−65.
9. Chen Q, Chen L, Wu X, Zhang F, Jin H, Lu C, et al. Dihydroartemisinin prevents liver fibrosis in bile duct ligated rats by inducing hepatic stellate cell apoptosis through modulating the PI3K/Akt pathway. *IUBMB Life* 2016;**68**:220−31.
10. Wang Z, Yang X, Kai J, Wang F, Wang Z, Shao J, et al. HIF-1alpha-upregulated lncRNA-H19 regulates lipid droplet metabolism through the AMPKalpha pathway in hepatic stellate cells. *Life Sci* 2020;**255**:117818.
11. Zhang Z, Yao Z, Wang L, Ding H, Shao J, Chen A, et al. Activation of ferritinophagy is required for the RNA-binding protein ELAVL1/HuR to regulate ferroptosis in hepatic stellate cells. *Autophagy* 2018;**14**:2083−103.
12. Gorgoulis V, Adams PD, Alimonti A, Bennett DC, Bischof O, Bishop C, et al. Cellular senescence: defining a path forward. *Cell* 2019;**179**:813−27.
13. Jun JI, Lau LF. Resolution of organ fibrosis. *J Clin Invest* 2018;**128**:97−107.
14. Krizhanovsky V, Yon M, Dickins RA, Hearn S, Simon J, Miething C, et al. Senescence of activated stellate cells limits liver fibrosis. *Cell* 2008;**134**:657−67.
15. Jin H, Lian N, Zhang F, Bian M, Chen X, Zhang C, et al. Inhibition of YAP signaling contributes to senescence of hepatic stellate cells induced by tetramethylpyrazine. *Eur J Pharmaceut Sci* 2017;**96**:323−33.
16. Jin H, Lian N, Zhang F, Chen L, Chen Q, Lu C, et al. Activation of PPARgamma/P53 signaling is required for curcumin to induce hepatic stellate cell senescence. *Cell Death Dis* 2016;**7**:e2189.
17. Malaquin N, Martinez A, Rodier F. Keeping the senescence secretome under control: molecular reins on the senescence-associated secretory phenotype. *Exp Gerontol* 2016;**82**:39−49.
18. Hoare M, Ito Y, Kang TW, Weekes MP, Matheson NJ, Patten DA, et al. NOTCH1 mediates a switch between two distinct secretomes during senescence. *Nat Cell Biol* 2016;**18**:979−92.
19. Ito Y, Hoare M, Narita M. Spatial and temporal control of senescence. *Trends Cell Biol* 2017;**27**:820−32.
20. Campisi J. Aging, cellular senescence, and cancer. *Annu Rev Physiol* 2013;**75**:685−705.
21. Nacarelli T, Lau L, Fukumoto T, Zundell J, Fatkhutdinov N, Wu S, et al. NAD^+ metabolism governs the proinflammatory senescence-associated secretome. *Nat Cell Biol* 2019;**21**:397−407.
22. Scalise M, Pochini L, Console L, Losso MA, Indiveri C. The human SLC1A5 (ASCT2) amino acid transporter: from function to structure and role in cell biology. *Front Cell Dev Biol* 2018;**6**:96.
23. Yang L, Venneti S, Nagrath D. Glutaminolysis: a hallmark of cancer metabolism. *Annu Rev Biomed Eng* 2017;**19**:163−94.
24. Lane AN, Higashi RM, Fan TW. Metabolic reprogramming in tumors: contributions of the tumor microenvironment. *Genes Dis* 2020;**7**:185−98.
25. Du K, Hyun J, Premont RT, Choi SS, Michelotti GA, Swiderska-Syn M, et al. Hedgehog−YAP signaling pathway regulates glutaminolysis to control activation of hepatic stellate cells. *Gastroenterology* 2018;**154**:1465−1479 e13.
26. Wiley CD, Velarde MC, Lecot P, Liu S, Sarnoski EA, Freund A, et al. Mitochondrial dysfunction induces senescence with a distinct secretory phenotype. *Cell Metabol* 2016;**23**:303−14.
27. Goodman ZD. Grading and staging systems for inflammation and fibrosis in chronic liver diseases. *J Hepatol* 2007;**47**:598−607.
28. Zhang Z, Guo M, Li Y, Shen M, Kong D, Shao J, et al. RNA-binding protein ZFP36/TTP protects against ferroptosis by regulating autophagy signaling pathway in hepatic stellate cells. *Autophagy* 2020;**16**:1482−505.
29. Kocabayoglu P, Lade A, Lee YA, Dragomir AC, Sun X, Fiel MI, et al. beta-PDGF receptor expressed by hepatic stellate cells regulates fibrosis in murine liver injury, but not carcinogenesis. *J Hepatol* 2015;**63**:141−7.
30. Wu X, Wu X, Ma Y, Shao F, Tan Y, Tan T, et al. CUG-binding protein 1 regulates HSC activation and liver fibrogenesis. *Nat Commun* 2016;**7**:13498.
31. Mederacke I, Dapito DH, Affo S, Uchinami H, Schwabe RF. High-yield and high-purity isolation of hepatic stellate cells from normal and fibrotic mouse livers. *Nat Protoc* 2015;**10**:305−15.
32. Li F, Huangyang P, Burrows M, Guo K, Riscal R, Godfrey J, et al. FBP1 loss disrupts liver metabolism and promotes tumorigenesis through a hepatic stellate cell senescence secretome. *Nat Cell Biol* 2020;**22**:728−39.
33. Jia Y, Wang F, Guo Q, Li M, Wang L, Zhang Z, et al. Curcumol induces RIPK1/RIPK3 complex-dependent necroptosis *via* JNK1/2-ROS signaling in hepatic stellate cells. *Redox Biol* 2018;**19**:375−87.
34. Zhang J, Zhou Y, Li N, Liu WT, Liang JZ, Sun Y, et al. Curcumol overcomes TRAIL resistance of non-small cell lung cancer by targeting NRH:quinone oxidoreductase 2 (NQO2). *Adv Sci* 2020;**7**:2002306.
35. Rezvani M, Espanol-Suner R, Malato Y, Dumont L, Grimm AA, Kienle E, et al. *In vivo* hepatic reprogramming of myofibroblasts with AAV vectors as a therapeutic strategy for liver fibrosis. *Cell Stem Cell* 2016;**18**:809−16.
36. Gu L, Kitamura M. Sensitive detection and monitoring of senescence-associated secretory phenotype by SASP-RAP assay. *PLoS One* 2012;**7**:e52305.
37. Herranz N, Gallage S, Mellone M, Wuestefeld T, Klotz S, Hanley CJ, et al. mTOR regulates MAPKAPK2 translation to control the senescence-associated secretory phenotype. *Nat Cell Biol* 2015;**17**:1205−17.
38. Yang C, Zeisberg M, Mosterman B, Sudhakar A, Yerramalla U, Holthaus K, et al. Liver fibrosis: insights into migration of hepatic stellate cells in response to extracellular matrix and growth factors. *Gastroenterology* 2003;**124**:147−59.
39. Johmura Y, Yamanaka T, Omori S, Wang TW, Sugiura Y, Matsumoto M, et al. Senolysis by glutaminolysis inhibition ameliorates various age-associated disorders. *Science* 2021;**371**:265−70.
40. Orjalo AV, Bhaumik D, Gengler BK, Scott GK, Campisi J. Cell surface-bound IL-1alpha is an upstream regulator of the senescence-associated IL-6/IL-8 cytokine network. *Proc Natl Acad Sci U S A* 2009;**106**:17031−6.

41. Lau L, Porciuncula A, Yu A, Iwakura Y, David G. Uncoupling the senescence-associated secretory phenotype from cell cycle exit *via* interleukin-1 inactivation unveils its protumorigenic role. *Mol Cell Biol* 2019;**39**.
42. Freund A, Orjalo AV, Desprez PY, Campisi J. Inflammatory networks during cellular senescence: causes and consequences. *Trends Mol Med* 2010;**16**:238−46.
43. Wang M, Hu R, Wang Y, Liu L, You H, Zhang J, et al. Atractylenolide III attenuates muscle wasting in chronic kidney disease *via* the oxidative stress-mediated PI3K/AKT/mTOR pathway. *Oxid Med Cell Longev* 2019;**2019**:1875471.
44. Huai B, Ding J. Atractylenolide III attenuates bleomycin-induced experimental pulmonary fibrosis and oxidative stress in rat model *via* Nrf2/NQO1/HO-1 pathway activation. *Immunopharmacol Immunotoxicol* 2020;**42**:436−44.
45. Schnabl B, Purbeck CA, Choi YH, Hagedorn CH, Brenner D. Replicative senescence of activated human hepatic stellate cells is accompanied by a pronounced inflammatory but less fibrogenic phenotype. *Hepatology* 2003;**37**:653−64.
46. Coppe JP, Kauser K, Campisi J, Beausejour CM. Secretion of vascular endothelial growth factor by primary human fibroblasts at senescence. *J Biol Chem* 2006;**281**:29568−74.
47. Huang F, Zhao Y, Zhao J, Wu S, Jiang Y, Ma H, et al. Upregulated SLC1A5 promotes cell growth and survival in colorectal cancer. *Int J Clin Exp Pathol* 2014;**7**:6006−14.
48. van Geldermalsen M, Wang Q, Nagarajah R, Marshall AD, Thoeng A, Gao D, et al. ASCT2/SLC1A5 controls glutamine uptake and tumour growth in triple-negative basal-like breast cancer. *Oncogene* 2016;**35**:3201−8.
49. Shimizu K, Kaira K, Tomizawa Y, Sunaga N, Kawashima O, Oriuchi N, et al. ASC amino-acid transporter 2 (ASCT2) as a novel prognostic marker in non-small cell lung cancer. *Br J Cancer* 2014;**110**:2030−9.
50. Liu Y, Yang L, An H, Chang Y, Zhang W, Zhu Y, et al. High expression of solute carrier family 1, member 5 (SLC1A5) is associated with poor prognosis in clear-cell renal cell carcinoma. *Sci Rep* 2015;**5**:16954.
51. Xu M, Pirtskhalava T, Farr JN, Weigand BM, Palmer AK, Weivoda MM, et al. Senolytics improve physical function and increase lifespan in old age. *Nat Med* 2018;**24**:1246−56.
52. Chang J, Wang Y, Shao L, Laberge RM, Demaria M, Campisi J, et al. Clearance of senescent cells by ABT263 rejuvenates aged hematopoietic stem cells in mice. *Nat Med* 2016;**22**:78−83.